Development of ultrathin delay line for attosecond resolved high harmonics and interferometric applications

Sunil Dahiya

A thesis submitted for the partial fulfillment
of the degree of Doctor of Philosophy

Department of Physical Sciences
Indian Institute of Science Education and Research Mohali
Knowledge city, Sector 81, SAS Nagar, Manauli PO,
Mohali 140306, Punjab, India.

November, 2022

Certificate of Examination

This is to certify that the dissertation titled **"Development of ultrathin delay line for attosecond resolved high harmonics and interferometric applications"** submitted by **Sunil Dahiya** (Reg. no. MP14014) for the partial fulfillment of Doctor of Philosophy program of the institute, has been examined by the thesis committee duly appointed by the institute. The committee finds the work done by the candidate satisfactory and recommends the report to be accepted.

Dr. Ramandeep Singh Johal Dr. Samir Biswas Dr. Kamal P. Singh

(Supervisor)

Dated: 30 November, 2022

Declaration

The work presented in this dissertation has been carried out by me under the guidance of Dr. Kamal P. Singh at the Indian Institute of Science Education and Research Mohali.

This work has not been submitted in part or in full for a degree, a diploma, or a fellowship to any other university or institute. Whenever contributions of others are involved, every effort is made to indicate this clearly, with due acknowledgement of collaborative research and discussions. This thesis is a bonafide record of original work done by me and all sources listed within have been detailed in the bibliography.

Sunil Dahiya
(Candidate)

Dated: 30 November, 2022

In my capacity as the supervisor of the candidate's doctoral thesis, I certify that the above statements by the candidate are true to the best of my knowledge.

Dr. Kamal P. Singh
(Supervisor)

Acknowledgments

I would like to express my sincere gratitude to my supervisor, Dr. Kamal P. Singh, for his guidance, help and encouragement throughout the duration of my doctoral thesis. I thank him for introducing me with field of attosecond science and providing opportunity to work on HHG setup which was designed and developed by him prior to my thesis work. I sincerely thank to my doctoral committee members, Prof. R.S. Johal and Dr. Samir Biswas for their valuable comments and support.

I would like to thank former member of lab Dr.M.S. Sidhu for providing fs laser beam time and suggestions regarding betterment of ATTO-setup from time to time. I also extend my thank for their input in paper writing and figures. I also thank former lab member Biplob Nandy to introducing me to the ATTO-setup and initial guidance at earliest stage of my thesis work. I also thank Chetna Taneja and Sanjay kapoor for their help in modifications at ATTO-setup.

I want to extend a special thank to Dr.Ankur Mandal for their contribution to the theoretical model of harmonics and white light fringes that helped us in validating the experimental results. I sincerely thank him for his insightful discussions and guidance for understanding different concepts of HHG and in other fields too. I heartily thank my colleague Akansha Tyagi for her consistent help and support in experimental work, framing the model for white light fringes and major inputs in paper writing and discussion.

I also thank my former and current lab members Dr. Komal Chaudhary, Shivali Sokhi, Varun Ranade, Dr. Bhavesh, Biswajit Panda, Jayant and Sandeep Jhakhar for making the healthy scientific environment in lab and providing help whenever required.

I am grateful to my parents, my wife (Shivali Sokhi) and all my family members for their motivation and hospitality in tough times.

I acknowledge IISER Mohali sports and cultural clubs specially basketball, cricket and bhangra club and their past and current members for a joyful environment throughout my PhD journey.

I gratefully acknowledge the funding received from IISER Mohali towards my PhD fellowship. I also acknowledge the IISER Mohali library for various scientific study.

Abstract

The study of light-matter interaction at an ultrafast time scale of femtosecond and attosecond is quite exciting and gives an understanding of quantum behaviour in atoms and molecules. A lot of efforts have been made regarding building up the tools and techniques to understand these interactions. Here, we are trying to develop a tabletop attosecond pulse source through high harmonics generation process in gases using a highly intense femtosecond laser. We aim to develop an optical delayline/interferometer capable of measuring and controlling attosecond resolved dynamics.

Optical delay lines with attosecond resolution and ultrahigh stability are the important tools of atto-science and technology for various applications such as characterization of ultrashort pulses and pump-probe spectroscopy in atomic and molecular medium. For attosecond controlled measurements of electron dynamics, it is necessary to have a reference of absolute-zero time delay which demands nanometer scale matching between the interferometer arms which is challenging with conventional designs having low stability and resolution. Hence, it is important to have a delay line with attosecond resolution and high stability providing zero delay reference for experiments using ultrashort pulses.

We have developed and realised a compact ultra-thin attosecond optical delay line of sub 10 attosecond resolution and around 2 attosecond stability providing time zero reference with negligible dispersion effects. The performance of the delay line is validated by observing attosecond resolved oscillations in the yield of high-harmonics induced by two time delayed infrared femtosecond pulses. This ultrathin delayline is also used as an autocorrelator to characterize the femtosecond pulses in the time domain. Also, we demonstrate a tunable wavefront split ultrathin white light interferometer enabling picometer resolution of optical path difference. We have used it for the measurement of temporal coherence length of several broadband incoherent sources as small as a few micrometers.

The presented design overcomes the major challenges in the existing delaylines for ultrafast attosecond measurements. This ultrathin delayline can be used with various applications in ultrafast science for attosecond resolved measurements such as photoionization of atomic and molecular systems.

Table of Contents

List of Figures

Most used abbreviations

HHG	High Harmonic Generation
IAC	Interferometric Autocorrelation
Laser	Light Amplification by Stimulated Emission of Radiation
BS	Beam Spliter
CCD	Charge Coupled Device
ND	Neutral Density
fs	Femtosecond
as	Attosecond
OPD	Optical Path Delay
XUV	Extreme Ultraviolet
IR	Infrared
FWHM	Full width at Half Maximum
OPD	Optical path difference
RABBIT	Reconstruction of Attosecond Beating By Interference of Two-photon transitions
NIR	Near Infrared
FRAC	Fringe Resolved Autocorrelation
ZPD	Zero Path Difference

Chapter 1

General Introduction

The invention and advancement of LASER (light amplification by stimulated emission of radiation) have made a great contribution to many research and engineering fields with its exceptional properties like coherence, tight spot focusing and high intensity. Lasers have a variety of applications in different areas like optical communications, laser cutting, LADAR (LAser Detection And Ranging) and in medical applications [1]. With the development of pulse laser, a new fields of study have emerged like non-linear optics, pump-probe spectroscopy, non-thermal ablation, soft tissue surgery, etc [2, 3]. While ultrafast femtosecond (fs) pulses have become an easy to use facility now-a-days, the quest for generating and controlling shorter pulses in attosecond (*as*) time domain has been still going on for the last two decades.

Multiple electron dynamics phenomena such as multiphoton ionization and tunneling ionization, occur at attosecond time scale and in order to capture or study these phenomenons, we need light pulses of similar order in time domain. One of the examples to give a quantitative estimate of as time is that according to Bohr's model of an atom, a hydrogen atom's electron completes one cycle of revolution in about 150 *as*. Though the probabilistic quantum mechanical model has replaced Bohr's model, quantization of the shell is still valid and gives an intuition of *as* time scale.
The pulse duration of a light pulse is inversely proportional to spectral bandwidth and is bound by the time bandwidth product i.e. $\delta\nu\delta t \geq 0.44$ for Gaussian pulse [2]. For a transform limited Gaussian pulse in energy terms, it can be written as, δE (eV) . δt (*as*) = 1825. Therefore, for pulses shorter than 1 fs, the spectral bandwidth should be larger than 1.8 eV and spectrum wings will be extended to 5.5 eV, which is much larger than the range of visible light [4]. For a 100 *as* pulse, this bandwidth range is around 18 eV and therefore, in order to obtain attosecond pulse duration, the pulse

has to cover the spectrum in UV or extreme UV regime.

There are a couple of ways to generate attosecond pulses such as high harmonic generation (HHG) [5, 6] and free electron laser (FEL) [7–9]. Though attosecond pulse generation from FEL requires a big facility providing higher intensity, a table top HHG setup remains a preferred and generic way of generating *as* pulses for ultrafast experiments. HHG involves a nonlinear frequency up conversion of fs near infrared (NIR) pulses and leads to generation of integer multiples of fundamental frequency called high order harmonics that lie in extreme ultraviolet (XUV) regime. It was first proposed in 1992 [10] that attosecond pulses can be produced via HHG phenomenon but experimentally observed and characterization was done in 2001 [6, 11]. A sequence of attosecond pulses is generated with a single fs pulse known as attosecond pulse train (APT) with discrete spectrum. The generation of coherent XUV radiation of APT via HHG home built setup and its reproducibility is an important research problem in this thesis.

The requirement of good interferometric stability and attosecond time delay from delaylines remains a challenging aspect in attosecond experiments. Delay lines are categorized as amplitude split and wavefront split of ultrafast pulses in order to provide controllable time delays. A number of delaylines based on amplitude split configuration are Michelson [12], Mach–Zehnder [13, 14] and spatial-light modulators [15]. These delaylines provide good resolution of time delay steps but poor stability. In order to stabilize these delaylines from path fluctuations, active stabilization techniques are used [16, 17] which make it a complex setup. On the other hand, wavefront split delaylines offer good stability due to common path configuration. Some of them are based on a pair of split-mirrors [18, 19] or a pair of mm-thick glasses [20, 21] configuration. Though split-mirror based delaylines provide attosecond stability, however demand specialized optics, careful fabrication and tedious alignment procedures [15, 22–24]. Also, obtaining a time zero delay reference at which both the interferometric pulses superimpose exactly in time, is challenging with above mentioned delaylines. Such time zero reference is crucial for attosecond control and measurements of electron dynamics [25]. This motivated us to develop a new delayline of *as* resolution and high stability with zero time delay reference.

Characterization of ultrafast pulses is an important task for such time resolved experiments. There are different techniques based on autocorrelator [26] and streaking [27, 28] existing for characterization of ultrafast pulses. Autocorrelator techniques are further divided into intensity autocorrelation, fringe resolved autocorrelation (FRAC)

or interferometric autocorrelation and frequency resolved optical gating (FROG) [29]. These autocorrelators need to be perfectly aligned in order to avoid any asymmetry in the autocorrelation signal. Further, most of the autocoorrelators use delaylines incapable of making dispersion free measurements of ultrafast pulses. Such drawbacks motivate us to develop a perfectly aligned and dispersion free autocorrelator for fs laser system and can be further used for characterization of attosecond pulses.

Another work of development of a new kind of white light interferometer is a part of the thesis. White light interferometry is a non-contact and non-invasive technique used for many applications such as surface profile measurements [30], vertical scanning interferometry [31], thin film characterization [32, 33], dispersion measurements of optics [34, 35] and characterization of coherence properties of different optical sources [36]. In white light interferometers, the condition of matching two arms of interferometer within its coherence length, is important. Many white light interferometers based on amplitude division of light beam such as Michelson, Mach-Zehnder, Mirau, Sagnac and Linnik setups [37–40] have difficulty of achieving zero optical path difference (OPD) condition and dispersion compensation. Though this difficulty of obtaining zero OPD condition is reduced for wavefront division based white light interferometers such as Young's double slit [38, 41] and fresnel bi-prism [41] yet they are unable to provide variable OPD and are limited to provide spatial coherence information of the light sources only. For quantitative measurements, high resolution of white light interferometer is needed which was achieved in picometer scale earlier by piezo-translation stages [42, 43] and are prone to interferometric path instability. Hence, a tunable OPD and wavefront split dispersion balanced white light interferometer with picometer resolution and stability will be a better choice to use it in existing white light interferometry applications.

Aims and objectives

- Optimizing a table top attosecond pulse laser source of light via high harmonic generation with fs pulses in atomic gas medium. For better reproducibility of HHG, its optimization is also an important goal.

- To develop tools or techniques to measure and control attosecond time dynamics. Regarding this, a new ultrathin delay line has been developed and experimentally realized in controlling the yield of high harmonics and attosecond time scale measurement.

- Application of delayline as dispersion free autocorrelator for characterization of fs pulses in time domain.
- Application of delayline as picometer resolved white light interferometer for measuring temporal coherence of various broadband sources of light.

With above listed objectives, we planned the thesis outlines in the following manner

In second chapter, the theory of generation of coherent XUV attosecond pulses via high harmonic generation is provided. To apply this nonlinear phenomenon in experiment, a home built table top attosecond pulse generation setup (ATTO-setup) is made in our lab. In brief, we observed high order harmonics of IR pulses (800 nm) even up to 29^{th} order with Argon (Ar) gas as a nonlinear medium. We further characterized the order of the harmonics order via transmission curve of Aluminium (Al) which act as a spectral filter. We optimized the system to maximize the yield of harmonics by varying different parameters like gas load pressure, input IR pulse energy and propagation vacuum. Multiple checkpoints and references along the fs beam line have been made to maintain reproducibility of high harmonics. Further, in order to pump-probe experiments with high order harmonics, we need a highly stable delayline with *as* resolution. This necessity leads us to develop a new delayline of our own.

In third chapter, we design and demonstrate a highly stable ultrathin delayline with attosecond resolution providing time zero reference. The ultrathin delayline concept is based on wavefront division of input fs pulse with upper and lower micrometer ultrathin glass plates and time delay between them is controlled via precise rotation of lower glass plate using a Thorlab's rotation motor. These ultrathin glasses offer negligible dispersion to fs pulses thus resulting in no effective change in pulse width of input fs pulses. The mathematical framework of time delay with rotated angle of glass plates is explained in detail. Furthermore, time delay induced with this delayline is calibrated using He-Ne laser and fs pulses.

Time delay varies non-linearly with rotation angle providing high resolution of time delay near zero angle of about 2.5 *as* and tens of *as* in higher angle range. Its resolution is experimentally verified with intensity oscillations of He-Ne laser fringes. A discussion on a number of noises associated with measurement of resolution data is also presented. This inline delayline directly provides zero delay reference by aligning

the two glass in parallel configuration. The zero delay is also ensured by measuring point of inversion symmetry of fs pulses interferogram. Further, delayline stability to path fluctuations is also experimentally checked using He-Ne laser and found to be around 2 *as* only due to common path configuration. Also, we experimentally observed the main factor for this fluctuation was our He-Ne laser intensity.

In order to pump-probe experiment with IR pulses, we used this ultrathin delayline for controlling the yield of high harmonics via IR-IR time delay. We placed this inline delayline directly in the fs beam without changing our beamline of ATTO-setup. We observed and analysed high order harmonics of IR pulses using Ar gas as a nonlinear medium. With IR-IR time delay in input fs pulses, the yield of high order harmonics varies periodically in correspondence to fs IR (800 nm) pulse cycle of 2.7 fs and validated by theoretical model. The harmonics yield also shows sub-fs oscillations which are resolved via fourier transform method.

In fourth chapter, we used ultrathin delayline as an autocorrelator for measurement of fs pulses in time domain. These ultrathin glass plate induce negligible broadening of input fs pulse width and is discussed in detail. We measured the 2nd order interferometric autocorrelation (IAC) or FRAC signal by using BBO (β-barium borate) acting as a second harmonic generation nonlinear medium in phase matching orientation and ultrathin delayline for time delay input fs pulses. We used IR (800 nm) fs pulses and corresponding blue colour signal is observed through ultrathin autocorrelator. The IAC signal shows a FWHM of 35.45 fs corresponding to 25.14 fs pulse width measurement with less than 1% error. Ultrathin autocorrelator have a direct benefit of observing blue colour fringes and can be useful for measurement a few cycle fs pulses.

In fifth chapter, we introduce an ultrathin glass based white light interferometer with picometer scale resolution of optical path difference. Negligible dispersion and directly obtaining zero delay path position makes the ultrathin delayline as a white light interferometer. It is a balanced interferometer and white light fringes are easily observed using a partially spatially coherent source and lens-chip imaging system. This interferometer is used for measuring temporal coherence of various light sources like tungsten and white LED and has been found to be in agreement with their theoretical value. The interferogram corresponding to these sources shows about 300 pm resolution in measurement of optical path difference. Further, slit size effect is discussed and measured the spatial coherence of white LED source and verified with

theoretical equation. In last, modifications in white light interferometer for cavity based measurements are presented.

In summary

In short, the thesis consists of development and optimization of a table top high harmonics XUV source (attosecond pulses) and different applications of a new delayline in HHG, in characterization of fs pulses and in white light interferometry are demonstrated.

In the first task, we developed a reproducible attosecond pulse generation setup (ATTO setup) via high harmonic generation phenomenon with fs IR pulses. The characterization and optimization of harmonics has been done which is an important goal to make our ATTO setup ready to use facility.

In the second task, We designed and realized a new ultrathin delayline for time resolved experiments. Further, it is used for controlling the yield of high order harmonics via IR-IR time delay of input fs pulses. Our work regarding this ultrathin delayline having tremendous resolution and stability that help us in experiment of attosecond resolved measurement.

Two applications of ultrathin delayline are further explored. First, a dispersion and alignment free ultrathin autocorrelator for measuring fs pulse in time domain. A second application is a tunable wavefront split ultrathin white light interferometer for measuring the temporal coherence length of various broadband sources like tungsten and white LED with picometer resolution.

Chapter 2

Generation of high order harmonics

2.1 Ultrashort pulses

Ultrashort pulses comprise of optical pulses having pulse width lesser than a picosecond (10^{-12}) time scale. These ultrashort pulses can't be measured directly via a fast photodetector due to electronic limit of order of 10^{-9} s and need different techniques of measurement as discussed later in chapter 4.
In time domain, an ultrashort pulse is generally described by time dependent electric field E(t) written as following

$$E(t) = E_0 f(t) \cos\phi(t) \tag{2.1}$$

where E_0 is the maximum amplitude of the pulse, $f(t)$ is slowly varying envelope and $\cos\phi(t)$ is fast varying oscillating part. The $f(t)$ envelope term determines the pulse width calculated as full width half maximum (FWHM) of the intensity of the pulse ($I \propto f(t)^2$). The envelope term is commonly used in the form of Gaussian function which is written as;

$$f(t) = \exp\left[-(\frac{t}{t_p})^2\right], \tag{2.2}$$

$$t_p = \frac{t_{FWHM}}{\sqrt{2\ln 2}}. \tag{2.3}$$

Using Taylor's expansion, the temporal phase term $\phi(t)$ can be written as,

$$\phi(t) = \phi_{CEP} + \omega_c t + \theta(t) \tag{2.4}$$

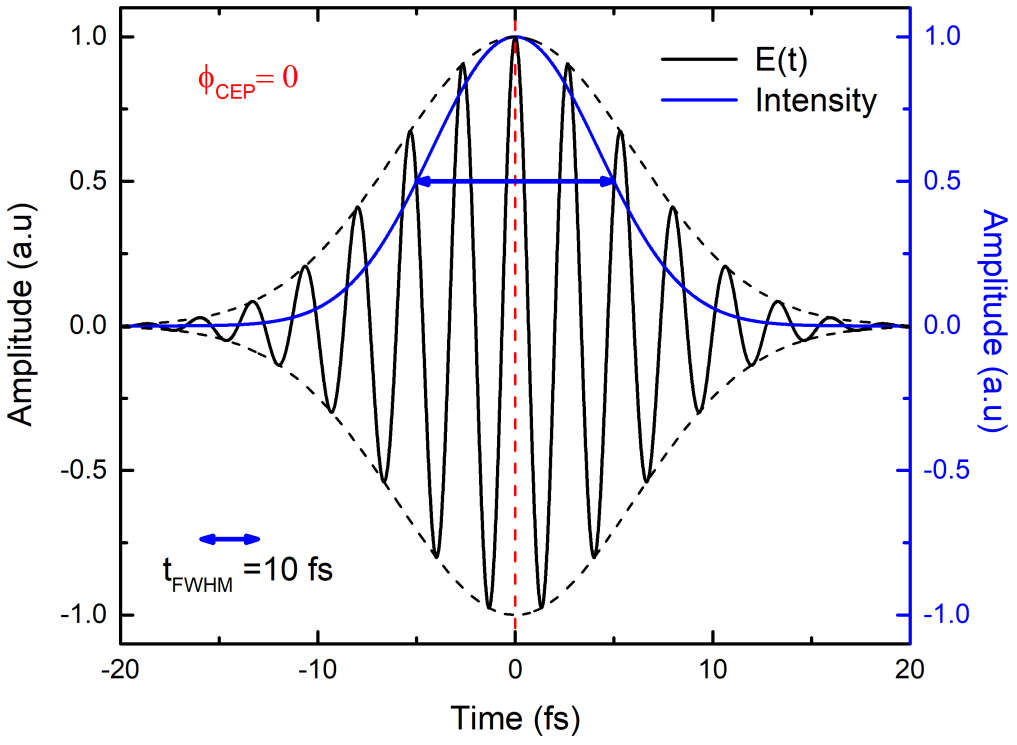

Figure 2.1: A Gaussian shaped pulse electric field (black line) with 10 fs pulse width (FWHM) having 800 nm central wavelength (ω_c = 2.35 $\times 10^{15}$ Hz) with $\phi_{CEP} = 0$ and $\theta(t) = 0$ is demonstrated. Also, intensity of the pulse ($\propto$E^2) (blue line) which is proportional to electric field showing FWHM 10 fs is plotted.

where ϕ_{CEP} is defined as the difference between the optical phase of the carrier wave and the envelope peak position phase value, ω_c is the central frequency and $\theta(t)$ contains the higher order terms of time (t^m, m$\geq$ 2). An ultrashort pulse in time domain is shown in Fig2.1 and its parameters are written alongside. The phase ϕ_{CEP} corresponds to difference between highest oscillation peak and the envelope peak. The instantaneous frequency is defined as time derivative of temporal phase,

$$\omega(t) = \frac{d}{dt}\phi(t) = \omega_c + \frac{d}{dt}\theta(t) \tag{2.5}$$

is non constant for $\theta(t) \neq 0$ which usually happens when an ultrashort pulse passes through a transparent medium resulting in a phase distortion called chirp. For m=2,

chirp is linear otherwise for m>2, chirp is nonlinear. Depending upon whether $\omega(t)$ increases or decreases with time, the pulse will have positive (up) or negative (down) chirp respectively. This chirp phenomena results in an increase in pulse duration.
The fourier relation or time bandwidth product for a Gaussian pulse is written as, $\delta\nu\delta t \geq 0.44$ where $\delta\nu$ is frequency bandwidth FWHM with $\omega = 2\pi\nu$ and δt is FWHM in pulse time. The equality holds in time bandwidth relation for non chirp pulses also called transform limited pulses by reaching the shortest pulse with a given bandwidth. Therefore, to go beyond a particular pulse duration, one has to enhance the the spectrum bandwidth. The idea of generating shorter pulses in attosecond domain lies here.
A number of nonlinear phenomenon are possible due to ultrashort pulses such as multiphoton ionization, frequency up conversion, kerr lens self focusing phenomenon etc [2, 44]. High harmonic generation is one of the non-linear frequency up conversion phenomenon with which we are able to increase frequency bandwidth in order to produce coherent pulses in the regime of attosecond. This method is discussed in detail in the next section.

2.2 Theory of high harmonic generation

The ultrashort fs pulses are capable of producing peak intensity of order of 10^{14} to 10^{15} W/cm^2 which is equal to high electric field strength of 10^8 to 10^9 V/cm. This is order of atomic unit of electric field (1 atomic unit of E = 5.14×10^9 V/cm). One atomic unit of electric field is magnitude with which an electron is bound within hydrogen atom. Then this high electric field cannot be treated perturbatively in such strong laser-atom interaction. High order harmonic generation is an example of a non perturbative nonlinear process in which intensity of higher order of harmonics (multiples of fundamental frequency) does not scale exponentially with harmonic order. The first high harmonic generation was independently observed by two groups around 1987 [45, 46]. After 4 to 5 years, it was possible to explain them with three step model [47, 48]. The semi-classical 3 step model in which electron propagates classically, is explained in Fig.2.2. The steps are as follows,

Step 1. Ionization : When a high magnitude electric field (10^9 V/m) interacts with an atom, it tilts the coulomb potential of that atom to one direction. Then there are chances of one or more electrons to come out via tunneling phenomenon and results in ionization of the atom.

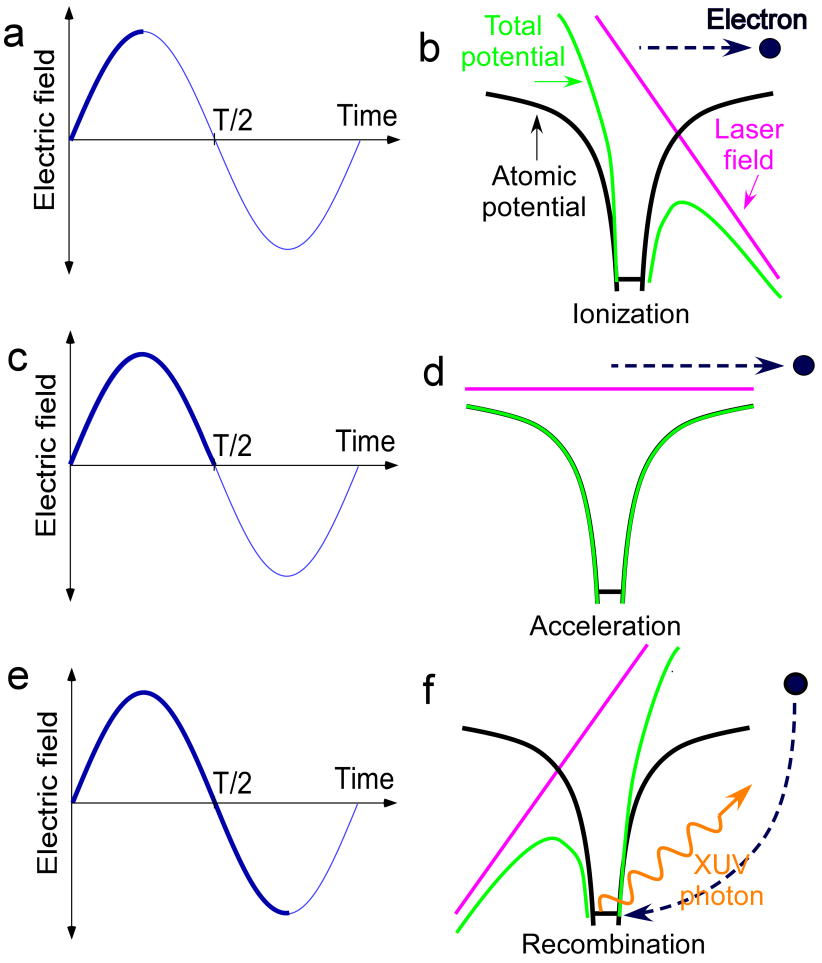

Figure 2.2: Illustration of 3 step model.

Step 2. Acceleration : The tunneled electrons still experience the electric field and accelerate in that medium resulting in gain of kinetic energy.

Step 3. Recombination : When the electric field's sign changes (from positive cycle to negative cycle or vice-versa), the free electron experiences force in other direction resulting in tilt of coulomb potential in other direction. Then there are chances of the electron to recombine with the parent ion and emit high energy radiation in XUV regime.

The energy of emitted radiation due to recombination is the sum of ionization energy and kinetic energy gained in the electric field. The maximum energy or cutoff energy of harmonic can be expressed as follows [4],

$$E_{max} = I_p + 3.17U_p \tag{2.6}$$

where I_p is the ionization energy of the atom and U_p is the pondermotive energy defined as average cycled kinetic energy gained by the electron in the presence of external field.

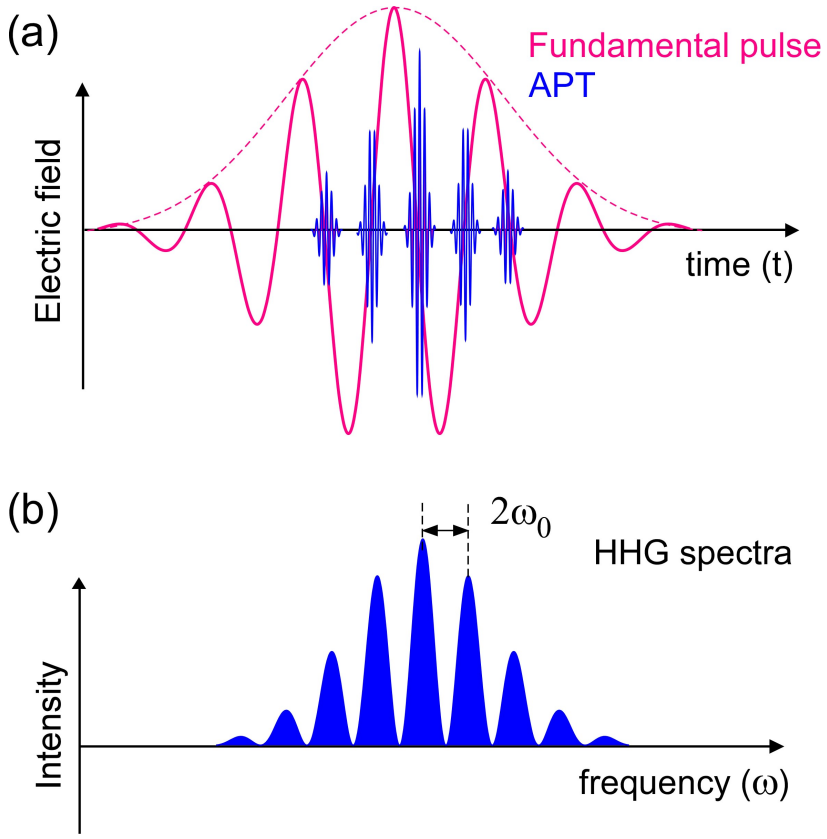

Figure 2.3: (a) Illustration of femtosecond pulse (fundamental) and generated attosecond pulse train (APT). (b) Fourier transform of APT leads to high harmonics spectra having $2\omega_0$ separation where ω_0 fundamental fs pulse central angular frequency.

$$U_p = \frac{e^2 E_0^2}{4 m_e \omega^2} \propto \lambda^2 I \tag{2.7}$$

From above equation, it is evident that maximum energy of XUV photons will increase with increasing wavelength and high intensity of the pulses for a given atomic system [4].

We usually use strong field IR pulses for such HHG phenomena. Due to symmetry of IR electric field oscillation, HHG occurs at each half cycle of an IR pulse resulting in emission of an attosecond pulse each time leading to attosecond pulse train (APT). Each attosecond pulse corresponds to an XUV supercontinuum but in case

of APT, interference between these XUV supercontinua results in harmonics in frequency domain. The phase matching conditions between the attosecond pulses play an important role in the harmonics properties [4]. Since time period of attosecond pulse emission is T/2 (T is time period of IR pulse), these harmonics are spaced by $2\omega_0$ in frequency domain (ω_0 is IR central frequency) as shown in Fig.2.3.

2.3 Design and development of HHG setup

We use ultrashort femtosecond pulses to generate high order harmonics. For this, we have a commercially available fs laser system in our lab, the Femtopower compact Pro from Femtolasers (now Spectra Physics) which provides sub-30 fs IR (800 nm) pulses at 1 kHz repetition rate. It can deliver maximum energy of 2 mJ from the amplified part of the system. When such ultrashort pulses are focused to about 100 μm spot size, the corresponding peak power density will be around 10^{15} W/cm^2. Such high irradiance is sufficient for high harmonic generation process to occur as we had discussed in earlier section.
Our femtosecond laser system consists of oscillator section and amplification section. The oscillator part delivers sub-10 fs pulses with high repetition rate of around 78 MHz but having energy of the order of 2 nJ (gives peak power density 10^9 W/cm^2 for a 100 μm spot size) which is not sufficient for HHG. These oscillator femtosecond pulses are generated by mode-locking the emitted spectrum of Titanium doped sapphire ($Ti : Al_2O_3$) pumped by a 532 nm high power continuous laser. The emitted spectrum has a very wide range from about 680 nm to 1130 nm.
The oscillator pulses are then amplified up to a maximum of 2 mJ using chirped pulse amplification (CPA) in multipass configuration [49]. The CPA process includes sub-10 fs oscillator pulses to stretch (chirp) in time of order of picosecond to avoid any damage to optical mirrors during amplification. These stretched pulses are propagated many times (9 times) through an amplification system pumped by high power Q-switched pump laser. Then these amplified stretched pulses are recompressed to deliver sub-30 fs with mJ energy having narrow bandwidth amplification in our system. The spectrum of amplified pulses is of central wavelength of 800 nm (corresponding to 1.5 eV energy of photons) and bandwidth of around 50 nm.

In this section, our focus will be to discuss the design and operation of Attosetup and understand its technological aspect. The high harmonic generation setup is a

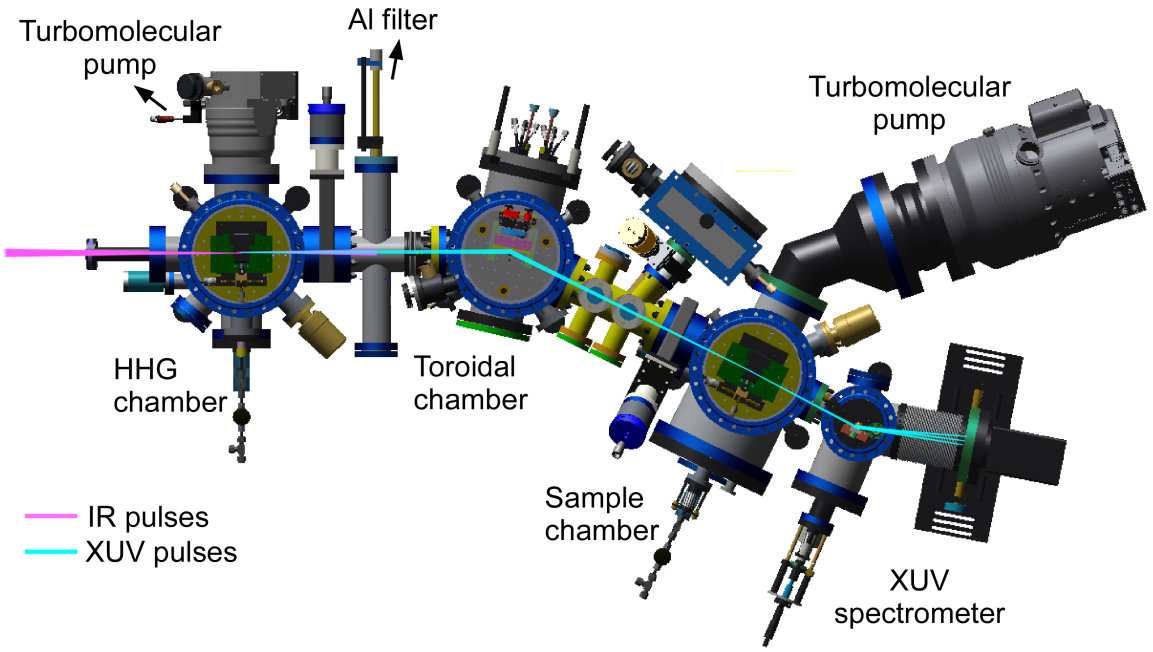

Figure 2.4: Topview of high harmonics setup (ATTO setup) in our lab showing different parts and components.

custom built one in our lab. The initial setup consisting of chambers and detectors were designed, developed and assembled before the beginning of this thesis work in lab. The schematic of HHG setup is shown in Fig.2.4 contains various components in order to generate and observe high order harmonics. In this Attosetup, several leak proof stainless steel (SS) chambers such as HHG chamber, Toroidal mirror chamber, sample chamber and turbomolecular vacuum pumps are there as shown in Fig.2.4. We need vacuum conditions in order to generate and propagate XUV photons of high energy ($>$ 10 eV) as they get easily absorbed in air by ejecting the valence electrons of atoms and molecules present. For example, Nitrogen gas is abundant in air and generated harmonics of XUV photons have energy way higher than ionization energy of most of gases present in air. The chambers are maintained at pressure of 10^{-8} mbar without gas load. The differential pumping method in which different chambers are connected with a narrow tube is used in setup to achieve high vacuum. Each chamber has a turbomolecular pump sufficient for maintaining ultrahigh vacuum.

In our setup, we use linearly polarised femtosecond infrared pulses (1 mJ, 25 fs) from the commercial system that are focused to gas capillary in the HHG chamber using a spherical concave mirror (f= 50 cm) as shown in Fig.2.5. Using this focusing

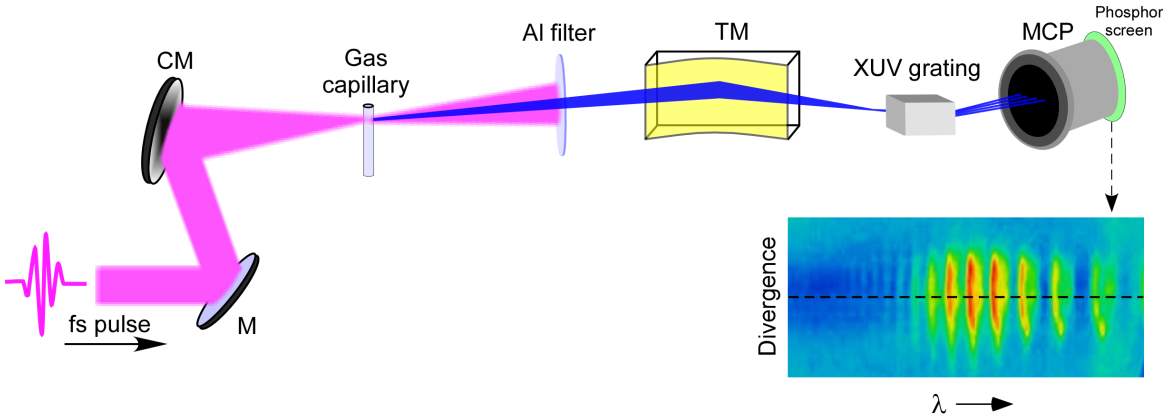

Figure 2.5: Schematic of fs beamline for HHG setup. The fs pulses are focused in gas capillary using f = 50 cm concave mirror. Al filter blocks the IR beam. The XUV spectrometer consists of a spherical XUV grating and a micro-channel plate (MCP) detector. A typical high harmonics observed on MCP detector in wavelength scale. M, plane mirror; CM, concave mirror; TM, toroidal mirror.

geometry, we are able to achieve peak intensity of around 4 $\times 10^{14}$ W/cm^2 for $\sim$ 100 μm focal spot size (diameter) which is sufficient for high harmonic generation. We used concave mirror instead of using lens for focusing purpose to avoid pulse width increment and chromatic aberration (can be used for sub 10 fs beamline also). Here, we took care of the astigmatism caused due to spherical mirror by making the fs beamline incident close to normal of spherical mirror.

In this setup, inert gases are commonly used as a generating medium due to their high ionization energy. We used Argon (Ar) gas having I_p = 15.8 eV to generate higher order harmonics. The gas cell or capillary having dimension of outer diameter (OD =3 mm) and thickness of 0.5 mm is used which is closed from top as shown in Fig.2.6. The fs pulses are able to drill a through hole in capillary with their high intensity and correspondingly XUV photons are generated along the incident fs beamline. A turbomolecular pump (pumping speed = 400 l/s) (Pfeiffer) is attached to HHG chamber in order to maintain pressure and compensate the gas leak through the holes on both sides of the capillary. This gas capillary is mounted on translation stage in order to move it along the beamline using vacuum compatible picomotors. The fine position control of capillary will help in optimizing the phase matching condition. It is placed around 1 mm after the focus position in order to get high cutoff of harmonics [50].

After the HHG chamber, a metal filter is placed in order to isolate the IR and

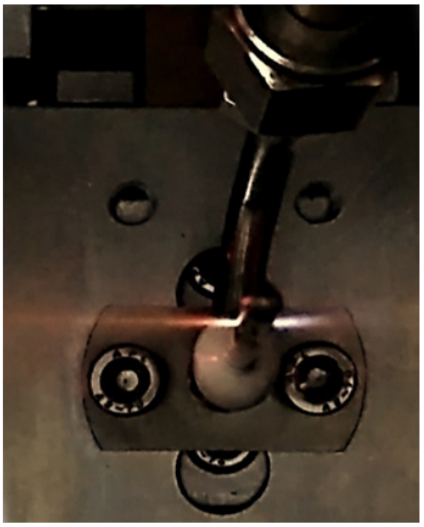

Figure 2.6: Ar gas filled capillary showing white light filamentation with XUV pulses generation.

XUV pulses. A 0.2 μm very thin Aluminium wrinkled filter (LEBOW) is used to block the IR beam (800 nm). It blocks lower order of harmonics/ photons having wavelength above than 80 nm and help us to calibrate harmonics order [4, 51]. It is kept in vacuum condition mostly as oxidation may occur in atmospheric air resulting in variation in its transmission properties [51].

After that, a toroidal mirror (f =25 cm) is placed at a distance of 50 cm from fs beam focus position making a 2f-2f geometry. It means, in a perfectly aligned system, toroidal focal spot size is same as concave mirror focal spot size. A toroidal shaped mirror is unique in sense that it provides astigmatism free focusing at a particular angle (in our case 76°) other than 0° from normal. It has two radii of curvature, one in horizontal plane and other in vertical plane. The detailed alignment can be found in this work [52]. The toroidal mirror has thin gold coating to reflect the high energy XUV photons to our sample chamber. The alignment of toroidal mirror beamline with Attosetup's central line is a crucial one in order to observe the harmonics on detector. For that, it is attached to a picomotor controlled mirror mount in order to tilt it in horizontal and vertical axis.

We measured the focal spot size of a He-Ne beam after toroidal mirror using Beam profiler (Thorlabs) and found out to be around 75 μm diameter (x-axis, $1/e^2$ Gaussian fitted), as shown in Fig.2.7(a). We also measured the various spot size in the Rayleigh

range and fit the following equation,

$$4\omega^2(z) = 4\omega_0^2[1 + \frac{\lambda}{\pi\omega_0^2}(z - z_0)^2] \tag{2.8}$$

where 2ω is beam diameter and $2\omega_0$ is beam waist (focal diameter) and λ is the wavelength of the ray. The above equation shows the variation in diameter of Gaussian beam and its good fit validate for astigmatism free focusing by toroidal mirror.

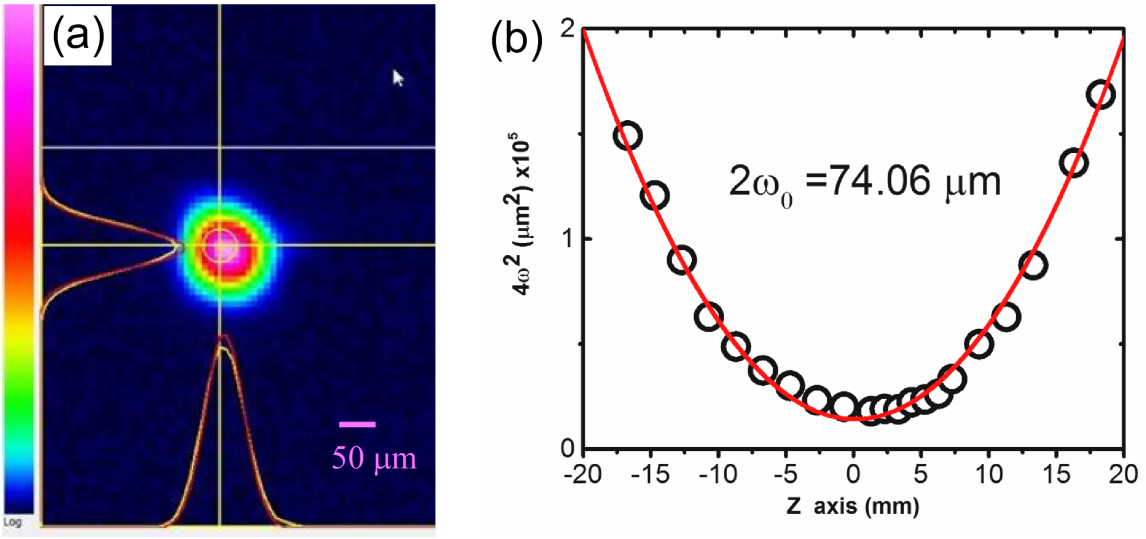

Figure 2.7: (a) He-Ne laser focal spot size captured after toroidal mirror using a Beam profiler (Thorlabs). (b) Variation of beam diameter (x-axis) along the propagation of laser beam (z-axis) and corresponding fit equation 2.8.

XUV spectrometer

Our XUV spectrometer consists of a spherical grating and a micro-channel plate (MCP) detector. In order to spectrally resolve the emitted harmonics or XUV radiation, a gold coated spherical concave grating (f=25 cm) is mounted in the beamline as shown in Fig.2.8. It is laminar curve variable line spacing (VLS) reflective grating (Shimadzu company) having 1200 groves/mm near center. It is placed at mechanical in/out assembly and attached with a picomotor mount for its tilt control. The spherical grating has a grazing angle of 3° for better efficiency in the resolved harmonics (Fig.2.8). It is similar to other gratings which distribute different colours or wavelengths in spatial axis.

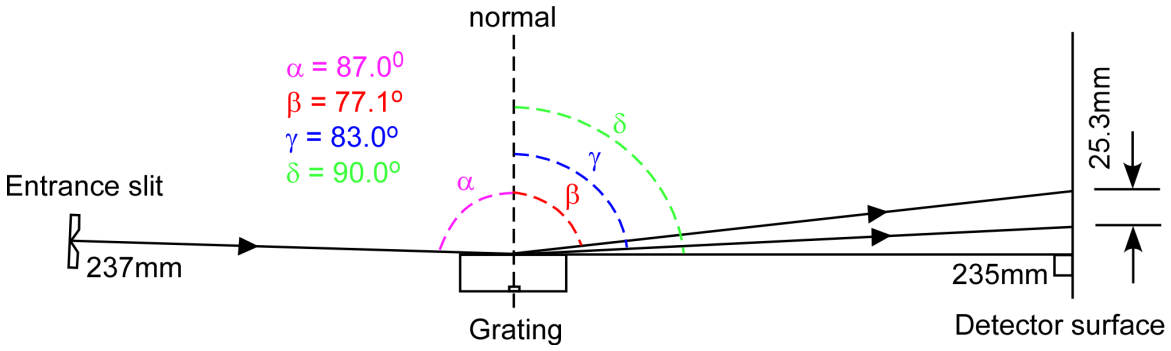

Figure 2.8: Diagram showing spherical grating position and corresponding angles for maximum intensity window of spectrally resolved harmonics. The entrance slit is referred to XUV beam focus position in sample chamber.

These spectrally resolved harmonics are observed on micro-channel plate (MCP) detector consists of a phosphor screen. It is a product commercially available from the Photonis company. A MCP is similar to a electron multiplier used to increase the gain for low intensity high energy (UV, XUV, X-ray) photons or electrons and ions. It is based on phenomenon of secondary emission of electrons. Our MCP is made of two planar plates aligned at a small angle to each other having hexagonal micro-size pore of 5 μm providing a gain (depends on biasing voltage) of around 10^3 from each plate. These secondary emitted electrons are made to fall on phosphor screen results in visible glow of harmonics intensity.

2.4 Optimization of harmonics

High order harmonics are observed on MCP detector as a result of high intensity fs pulses interaction with Ar gas. Harmonics are captured via a wide angle camera (Thorcam) for further analysis. In order to obtain better repeatability of harmonics, HHG is to be optimized with several parameters such as incident energy or power of fs pulses, Argon gas load in the capillary and propagation pressure.

Input fs power variation

With increase in fs laser average power, the peak intensity at the focal volume increases linearly. While pondermotive energy $U_p \propto$ I , there should be increase in maximum energy or cutoff threshold of harmonics as shown in Fig.2.9. Also, the yield

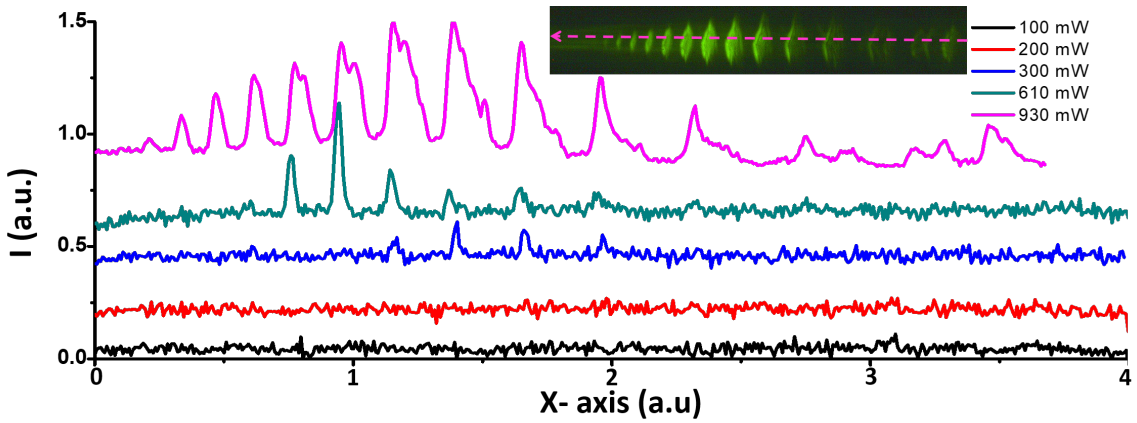

Figure 2.9: Variation of intensity of high order harmonics with input fs pulse average power is shown here.

or intensity of high harmonics increase corresponding to fs power increment. We used a neutral density (ND) filter in order to vary the average power of incident pulses. Here, we remain in tunneling regime (Keldysh parameter < 1) even for fs pulses of 1 Watt power in our setup.

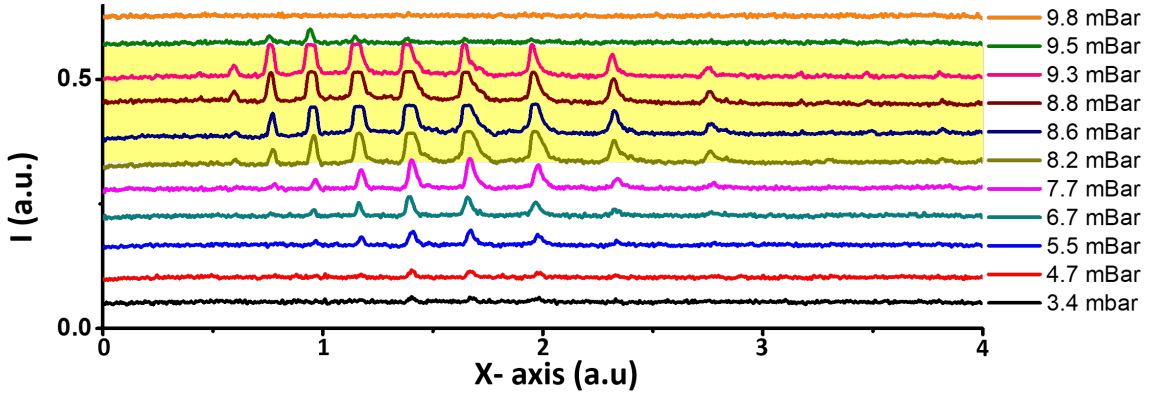

Figure 2.10: Variation of intensity of harmonics with Ar gas load is shown here. An optimum window (yellow) showing the maximum intensity of harmonics

Gas load and propagation pressure

With increase in Ar backing pressure or load, fs pulses will interact with higher density of atoms leading to high yield or intensity of high order harmonics. The macroscopic

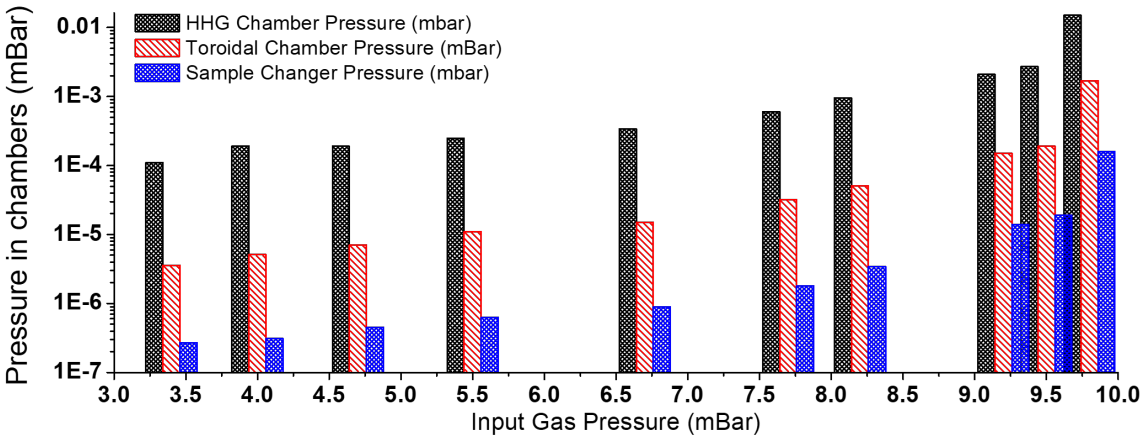

Figure 2.11: Variation in different chamber pressures with gas load at 0.6 mJ fs pulse energy.

phase match conditions will get better with increase in gas load and depend quadratically on pressure of the gas [50]. The variation of harmonics intensity with backing Ar gas pressure at 0.6 mJ of input fs pulses energy is shown in fig.2.10. There is an optimum window of gas load i.e. from 8.2 mbar to 9.3 mbar, harmonics yield is maximum for our setup conditions. Beyond 9.3 mbar Ar gas pressure, the process of re-absorption of generated XUV photons will dominate. With gas pressure, leak rate from the capillary's hole will become higher and correspondingly result in lowering the propagation vacuum as shown in Fig.2.11. As we can see, there is sudden increase in pressure of all chambers beyond 9.5 mbar of gas load that leads to absorption of XUV photons along propagation. Hence, there is a trade off between gas load and propagation pressure in order to optimize the harmonics.

2.5 Characterization of harmonics

With sufficient intensity of order of 10^{14} W/cm^2 and high precision in beamline alignment, high order harmonics are observed on phosphor screen (MCP detector) and captured using a camera (Thorcam). After optimization, the next task is to characterize the harmonics denoting the order number of individual harmonics. For this, we used Al filter beamline in or out technique to specify the order of harmonics. As per Fig.2.12, Al filter blocks the photons of higher wavelength of 80 nm i.e. upto 10^{th} harmonics (800 nm corresponds to fundamental frequency). With odd order of harmonics has to be observed due to symmetry reasons (as discussed in section 1.2),

upto 9^{th} order of harmonics are absorbed by Al filter. This helps us in characterizing the harmonics order as shown in Fig.2.13 for two different energy of incident fs beam of 0.9 mJ and 0.6 mJ. In Fig.2.13, for X > 2.5 a.u., we see detector noise data in this range and the first clear peak (with Al filter) gives the indication of 11^{th} harmonic. We were able to observe 29^{th} order of harmonics with Ar gas with 0.9 mJ input fs pulses.

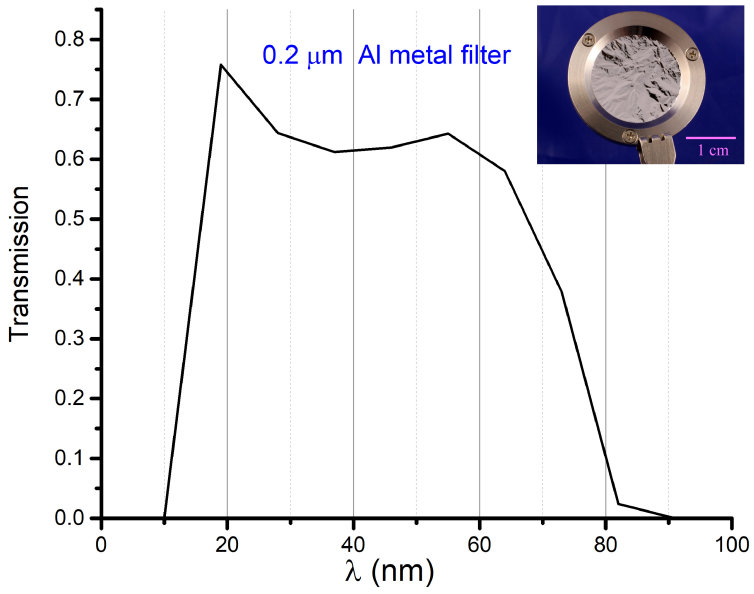

Figure 2.12: Transmission curve of a 0.2 μm thin aluminium (Al) filter. Inset: Real picture of Al filter used to block IR beam.

Here, the characterization of the harmonics in time domain could not be completely done in absence of crucial components at our setup due to its initial stage. In order to complete this task, we wish to incorporate instruments and techniques like velocity map imaging (VMI) and magnetic bottle electron spectrometer (MBES) in our setup in future for photo-electrons measurement. Further, we would like to characterize attosecond pulses via RABBIT (reconstruction of attosecond beating by interference of two-photon transitions) technique [6, 53].

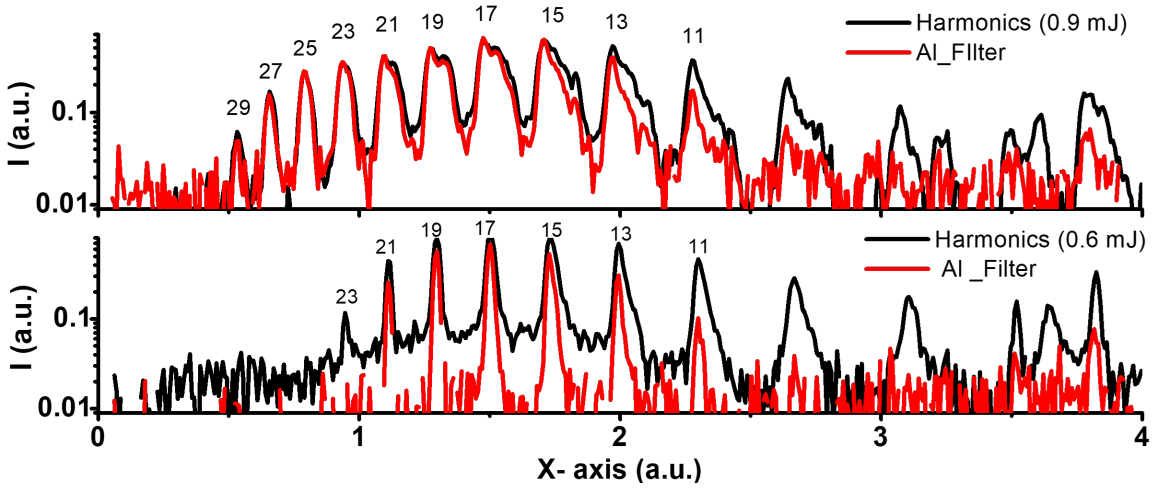

Figure 2.13: Characterization of harmonics with inserting Aluminium (Al) filter (Lebow 200 nm(thickness)) in the XUV beam path for 0.9 mJ and 0.6 mJ incident fs pulses beam. The Al-filter doesn't allow the harmonics above 80 nm or upto 9th harmonics are absorbed as observed in plot. Note that Al filter intensity is multiplied 6 times in order to compare the peaks.

2.6 Conclusion

In this chapter, we discussed the theory and experimental aspects of high harmonic generation phenomenon. The 3 step model explains the theory behind the HHG in detail. After that, various conditions such as high intensity of terawatt/cm^2, ultrahigh vacuum for XUV photons propagation ($\sim 10^{-8}$ mbar achieved) and sufficient gas load ($\sim$ 8 mbar in our case) which are necessary to generate and observe the high order harmonics are fulfilled. There are different technical challenges that we have overcome in this Attosetup. Some of them are high precision beam alignment, toroidal mirror astigmatism free focusing, XUV spectrometer alignment and maintaining ultrahigh vacuum. A detailed technical understanding of different of parts of Attosetup is presented in this chapter. We succeed in generating and observing harmonics of fs IR (800 nm) beam with Ar gas upto to 29^{th} harmonics order (for 0.9 mJ IR pulses). In order to attain repeatable harmonics, they are optimized for various parameters like gas load, driving fs pulses average power and propagation pressure. The observed harmonics are also characterized by their order number with the help of thin metal filter i.e. Al filter. This Attosetup provides coherent XUV pulses in attosecond time domain that can used in measurements of time dynamics in atomic and molecular systems.

Chapter 3

Ultrathin attosecond delay line

3.1 Introduction

Ultrafast delaylines are the key tools for time resolved experiments with ultrafast pulses and pump probe spectroscopy [18, 54, 55]. Such experiments demand attosecond time delay control of probe pulse and hence the requirement of attosecond delay controlled delayline arises with it.
A variety of delaylines with different designs based upon amplitude splitting are, Michelson [12] and Mach–Zender [13, 14]. The most common problems with these delaylines are precise delay control of attosecond time step and the path fluctuation/jitter between the pump and probe beams. For small displacements changes or fluctuation in relative paths (for example, ∼30 nm corresponds to a 100 as) will introduce a huge time lag between pump-probe pulses in attosecond time scale. These small scale path fluctuations are caused by various factors such as beam pointing instability, thermal and mechanical vibrations due to turbo mechanical pumps, water chillers needed for turbomolecular pumps and air flow by cooling fans associated with the setup.

Most of above mentioned amplitude split designs need active stabilization [16, 17] which increases the complexity of the setup with extra electronics having feedback controlled instruments. To avoid this complexity, passive stabilization using wavefront division designs such as a pair of split mirrors [18, 19], dual mirror setup [56] and a pair of mm-thick glass [20, 21] are explored. Though these wavefront delaylines provide attosecond stability, however demand specialized optomechanics fabrication

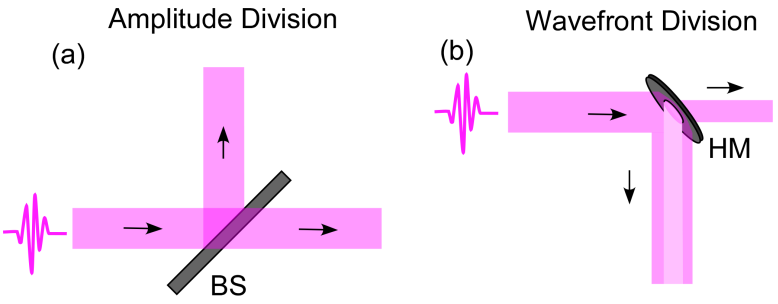

Figure 3.1: Schematic showing amplitude division (a) and wavefront division (b) incident pulse laser beam. BS, beam splitter; HM, holed mirror.

and tedious alignment. Hence, a direct easily aligned delayline with attosecond resolution and stability is crucial to develop for our setup applications.

3.2 Concept of ultrathin delayline

Rotation of glass is one of the simple methods to obtain very small and precise control of optical path delay [57]. With rotation of glass, light has to travel an extra path length in glass due to property of rectilinear propagation of light and different propagation speed of light in air and glass medium. Therefore, extra path length can be controlled via precise rotation of the glass plate and same is used for developing ultrathin glass based delayline.

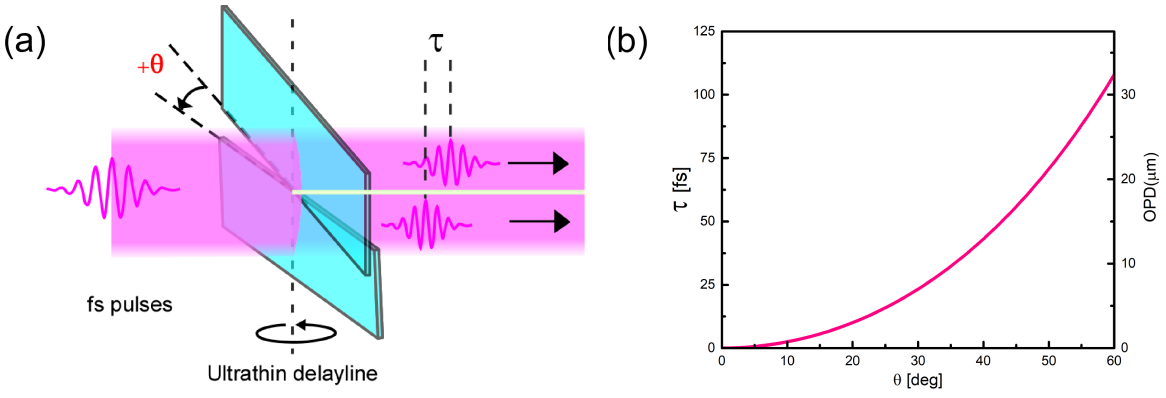

Figure 3.2: (a) Schematic of ultrathin delay line having upper and lower glass plate. Rotation of lower glass plate induces time delay τ between the two paths for an incident pulse laser beam. (b) Time delay (τ) and OPD versus angle of rotation graph are shown here for t=140 μm and n=1.52 obeying equation 3.1.

The corresponding time delay (τ) induced when glass plate is rotated (derivation in appendix), is written as follows.

$$\tau(\theta) = \frac{t}{c} \times [\sqrt{n^2 - \sin^2\theta} - \cos\theta - (n-1)] \tag{3.1}$$

where c is speed of light in air, n is the refractive index of glass material and t is thickness of the glass plate. θ is angle of rotation of glass plate with respect to (w.r.t.) normal position as shown in Fig.3.2(a). The net optical path difference (OPD $=\Delta D = c\tau$) is difference between the path induced by rotated lower glass plate with angle θ and path induced by upper glass plate at normal position to incident beam with at 0° angle. The graphical representation of τ and OPD versus angle θ is shown in Fig.3.2(b). We can see that τ is nonlinear curve with angle showing very small change in magnitude occurs near zero angle. It also provides a sufficient range of time delay ($\sim$ 100 fs for 60°) to have complete separation between two 25 fs (FWHM pulse width) pulses.

The above equation 3.1 can be written in a simple form for small angle by using Taylor series expansion. Upon solving the equation (in appendix), odd powers of θ vanish and upon truncation;

$$\Delta D(\theta) = \frac{(n-1)t}{2n}\theta^2 + \frac{(4n^2 - n^3 - 3)t}{24n^3}\theta^4 \tag{3.2}$$

However, θ^4 term is very small compared to θ^2 term and can be neglected for small angle. We can see that OPD depends quadratically on rotated angle θ,

$$\Delta D(\theta) = \frac{(n-1)t}{2n}\theta^2. \tag{3.3}$$

The above equation gives direct relation between angle of rotation and optical path difference for known thickness and refractive index of glass plate.

One important phenomenon is lateral or transverse shift (δs) of light when it passes through a rotating glass. The maximum lateral shift of the beam can be 140 μm at 90° (appendix) which is too small compared to the beam size of our fs beam i.e. 12 mm. Also, when incident beam is focused, this shift will change into even smaller angular change of order of δs (in μm)/ f (in cm). Hence two time delayed parts of the beam from our delayline maintain good spatial overlap at the focus position.

Another important phenomenon with glass plate is dispersion and its effect on pulse width broadening and chirp of the pulse. We calculated the first order ($dn/d\lambda$) and

second-order dispersion $d^2n/d\lambda^2$) with the ultrathin BK7 glass (t=140 μm). The first-order dispersion is $dn/d\lambda \sim 0.04\ \mu m^{-1}$ for the glass [58]. The group delay dispersion (GDD) [58] (GDD = t x GVD) is about 9.8 fs^2 at 0° and 10.29 fs^2 at 30° using group velocity dispersion (GVD) ,

$$GVD = \frac{\lambda^3}{2\pi c^2} \times \frac{d^2n}{d\lambda^2}. \tag{3.4}$$

Here, λ is the central wavelength of light passing through a transparent medium. The calculations suggest that there is a very small change in GDD value of below 0.5 fs^2 with rotation suggesting negligible dispersion effects.
We also calculated the corresponding pulse width change using glass plate. The pulse width after transmission through a medium of length L can be calculated [59] by

$$\tau(L) = \tau_0 \sqrt{1 + (\frac{8aL \times ln2}{\tau_0^2})^2} \tag{3.5}$$

where a is GVD/2 of the medium and τ_0 is initial pulse width. A 25 fs pulse width broadens only by around 0.01 fs while passing through a 140 μm BK7 glass (GVD = 44.65 fs^2/mm at λ = 800 nm) and hence pulse width broadening and chirp can be neglected for such ultrathin glass plates used for our delayline.

3.3 Ultrathin delayline setup

In this section, we introduce an ultrafast (fs) pulse wavefront split delay line with the help of ultrathin glass plates. The schematic diagram of our ultrathin delay line is shown in Fig.3.2(a). A pair of identical ultrathin glass plates (t=140 μm) is used for wavefront division purpose. These glass plates are placed vertically such that light (fs pulses) get spatially split symmetrically after transmission. These flat glass plates are held tight with a 3D printed frame to avoid any bending. The vertical gap between these glass plates is kept at less than 140 μm and checked by placing another replica of glass plate in between them. Either of the glass plates can be independently rotated precisely in order to provide optical path delay. In our case, we rotated lower glass plate using a motorized rotation stage connected at the central vertical axis of the glass plate. Rotation of lower glass plate provides optical path delay with respect to upper plate.

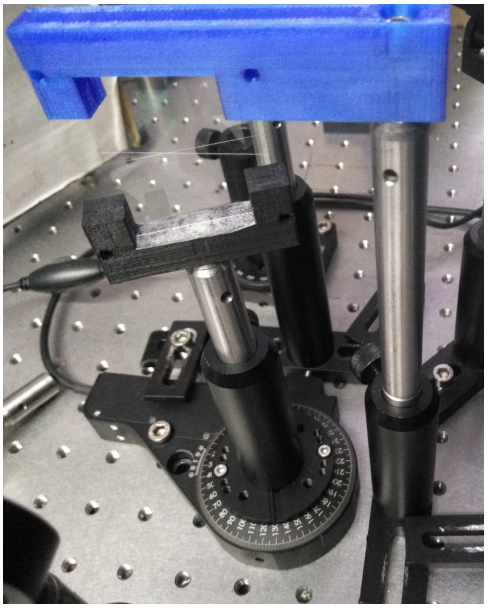

Figure 3.3: Photograph of ultrathin glass based delayline along with central axis of lower glass connected to a motorized rotation stage.

Interferometer design

The detailed description of glass properties, its outer glass frame and rotation stage is discussed in this section.

Glass properties

We used ultrathin cover glass (Blue star) as glass plate of 140 $\pm$ 10 μm thickness coarsely measured with a screw gauge [60]. Further, thickness measurement is validated from interferometric calibration discussed in detail in next section. These glasses lie in category of borosilicate (BK7) [60] having refractive index of 1.516 for 632 nm wavelength of light. Its dimensions were 22$\times$40 mm. The idea behind the use of these ultrathin glass was their common availability and high transmissivity to visible and IR rays (around 95%). One can use thinner glass commercially available of 30 μm thickness to minimize optical delay step [61].

Outer frame

The U-shaped mount of ultrathin glass plate has been made by 3D printer with precise depth according to the glass plate thickness. The ABS filament-based mount helps hold the glass plate vertically straight [62]. Initial angle or tilt in glass if any, was

checked with laser reflection spot at large distance. If a 3D printer is not available, one can paste these thin glasses to a opto-mechanical post to make such configuration. The lower glass U-shape mount is then connected to opto-mechanical post via a threaded screw at center. While upper glass is connected at one end to control them independently as shown in Fig.3.3.

Rotation motor

We used Thorlab motorized rotation stage (Thorlabs PRM1Z7) on which lower glass plate is mounted. This Thorlab's apt software controlled stepper motor can rotate with an angle of 0.0003^0 as minimum step increment or resolution of rotation stage. Its angle range and angular speed can be modified according to the user. One can use other continuous DC stepper motors [57].

3.4 Calibration of time delay of ultrathin delay line

The calibration of a delay line is an important task and need to be experimentally validated. Firstly, this delayline is used with a monochromatic source of light. This will help in self-calibration of the interferometer i.e. angle into displacement/time delay conversion.

3.4.1 Calibration using He-Ne laser

A He-Ne laser (Thorlabs) is incident on delayline which spatially split into two interferometric paths. The two split beams from the delayline are focused with a convex lens (f= 25 cm) resulting in the formation of interference fringes at the focal plane. These fringes are due to superposition of two coherent upper and lower part of spatial (XY) profile of laser beam. Interference fringes formed near focal plane are captured directly on a camera chip as shown in Fig.3.4. We used a simple webcam (QHM495LM) as our fringe detector. In Fig.3.4, the central part of He-Ne fringes shows interference between two split beams which vary from bright to dark with rotation of the glass plate. While the outer part shows the static fringes resulting from diffraction from the sharp edges of glass plates.

Starting from one side to another, we rotated the lower glass plate with constant angular speed of 0.5°. Here, we limit the maximum rotation angle to 60° due to loss of intensity at higher angle [57]. He-Ne interference fringes are video recorded.

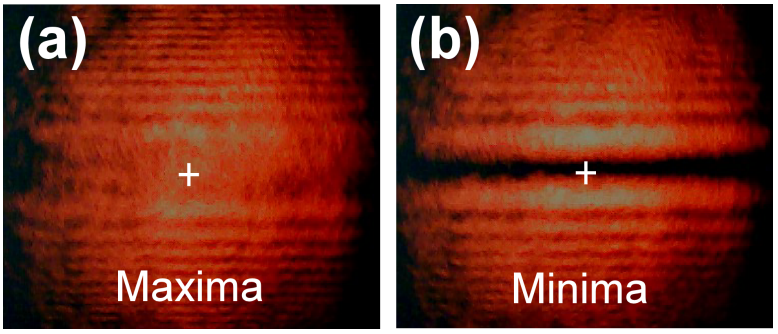

Figure 3.4: Experimental He-Ne laser interference fringes captured at camera chip using ultrathin delayline. Constructive (maxima) interference (a) and destructive (minima) interference (b) is formed during rotation of the lower glass plate. The cross-hair position showing the intensity tracked area.

Then fringes are intensity tracked in central area for a small area comprising of a couple of pixels (kept tracked area smaller than fringe width) as shown in Fig.3.4. This intensity is analyzed using Tracker software [63]. The corresponding He-Ne laser intensity oscillation of the interferometer also called interferogram is shown in Fig.3.5(a). In this graph, video time (t') is converted to angle rotated with a relation t' = $\theta/2$ as continuous angular speed was 0.5°/s.
For angle to path delay conversion, the intensity obtained with angle variation is fitted with the following equation,

$$I(\theta) = I_0 \cos^2(\frac{2\pi}{\lambda} \times OPD), \tag{3.6}$$

whereas OPD can be written using equation 3.1,

$$OPD = t \times [\sqrt{n^2 - \sin^2(\theta - \theta_0)} - \cos(\theta - \theta_0) - (n-1)]. \tag{3.7}$$

In Fig.3.5(a), the above equation is fitted with experimental data having fitting parameters wavelength (λ) = 632 nm, refractive index (n) = 1.516 and thickness of glass plate = 140 μm and angle offset (θ_0) = -0.047°. The fitting curve on experimental data is plotted using Wolfram Mathematica software (version 11.0) [64]. Using fitting parameters, the rotation angle θ is then converted into optical path delay according to equation 3.7 and the corresponding interferogram with OPD is shown in Fig3.5(b). To verify the time delay or OPD calibration, the minima values (separated by $\lambda = 632$ nm) taken from the interferogram in Fig. 3.5(a) are plotted with theoretical time delay curve which shows a good match as shown in Fig.3.6. Thus delayline self-calibrate

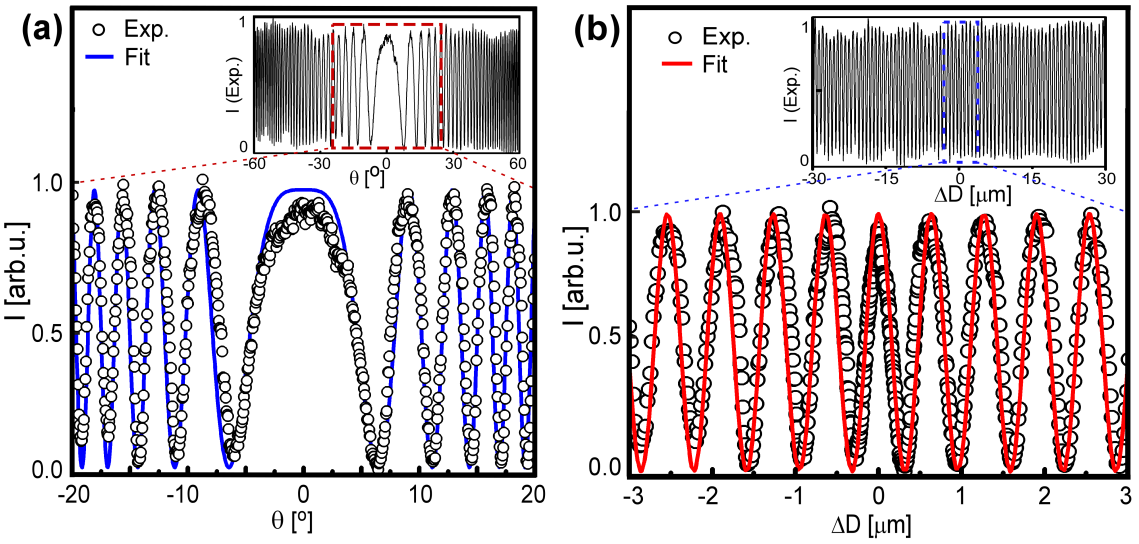

Figure 3.5: (a) Experimental and fit curve (equation 3.6) for angle range 0^0 to 20^0 is shown here. Inset: He-Ne intensity plot with angle rotation of lower glass plate from -60^0 to 60^0 relative to upper glass. (b) He-NE laser intensity and its fit after angle to OPD conversion using equation 3.6. Inset: He-Ne laser intensity with OPD conversion over large range from -30 μm to 30 μm.

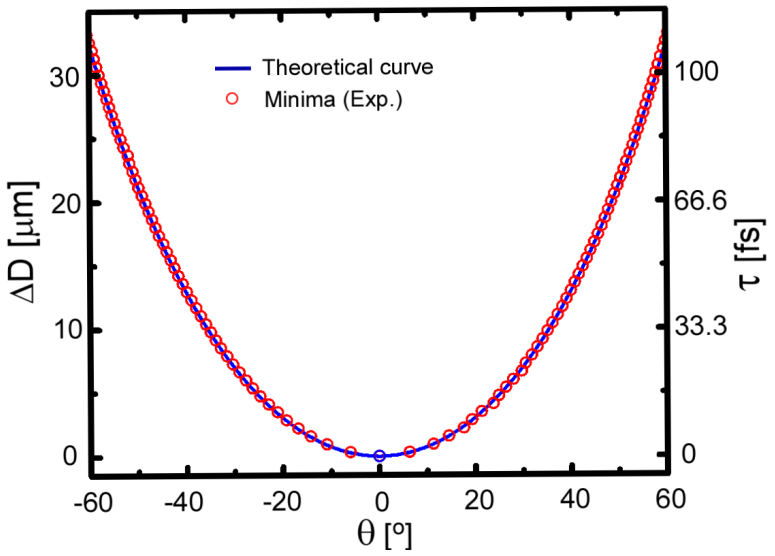

Figure 3.6: Calibration of optical path delay ΔD versus rotation angle θ for t=140 mm and n= 1.516. Solid line (blue) is theoretical curve corresponding to equation 3.7 and experimental data (red dots) corresponds to minima values of He-Ne laser interferogram having $\lambda = 632$ nm separation.

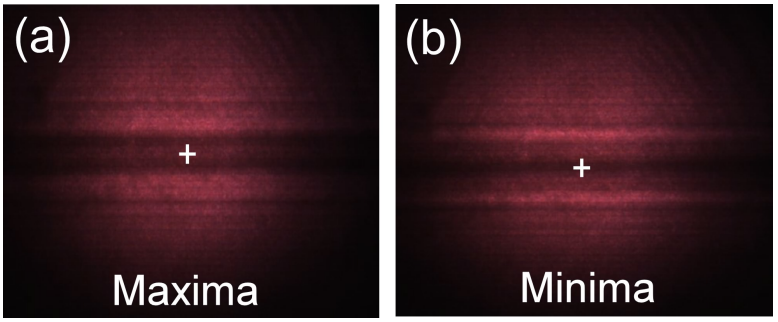

Figure 3.7: Image of the interference fringes ((a) constructive and (b) destructive) with fs pulses formed with ultrathin dealyline. They are captured on the screen at a 50 cm distance from delayline via a camera. The cross mark shows the intensity tracked area for interferogram.

θ in terms of OPD as fringe intensity obeys interference condition i.e. maxima (bright fringe) become minima (dark fringe) when optical path difference changes by $\lambda/2$.

3.4.2 Calibration using fs pulses

In this section, ultrathin delayline is used with fs pulses and a corresponding first order interferogram is obtained in order to validate the calibration. The fs beam interference fringes are directly observed on a screen after passing through ultrathin delayline (focusing these pulses will lead to burn the camera chip). These two fs pulse wavefront split paths overlap in space due to diffraction from glass plate sharp edges and form interference fringes in central area as shown in Fig.3.7.

By varying rotation angle θ of lower glass plate, intensity oscillates in the central region producing maxima and minima of interference pattern. The interference fringes are captured with a camera. The Fig.3.8(a) shows the central fringe intensity $I(\theta)$ variation with angle θ where the intensity varies faster for large angle due to nonlinear dependence of $\Delta\tau$ on θ. Also, we see that maximum intensity of fs fringes decreases with increase of rotation angle which is the effect of fs pulse envelope. Intensity variation of fs fringes using ultrathin delayline follows the following equation (detail in appendix),

$$I(\theta) = I_0[1 + e^{-(\frac{\tau(\theta)}{t_c})^2}\cos(\omega_0\ \tau(\theta))], \tag{3.8}$$

where $f(t) = e^{-(\frac{\tau(\theta)}{t_c})^2}$ is Gaussian envelope function of pulse, $\tau(\theta)$ is angle dependent time delay given by 3.1, t_c corresponds to pulse duration and $\omega_0 = 2\pi c/\lambda_0$. Using interference condition, the maxima become minima for $\Delta D = \lambda_0/2$ with the central

wavelength ($\lambda_0 = 800\ nm$) allowed us to self-calibrate θ versus τ. With rotated angle to time delay conversion according to equation 3.1, we obtain intensity variation of fs pulses with respect to time delay (τ) as shown in the Fig.3.8(b). This interferogram shows intensity oscillations of time period of around 2.7 fs which corresponds to $\lambda_0 = 800\ nm$, thus validates our calibration of delayline with fs pulses. This time dependent interferogram can also be termed as first order autocorrelation of fs pulses.

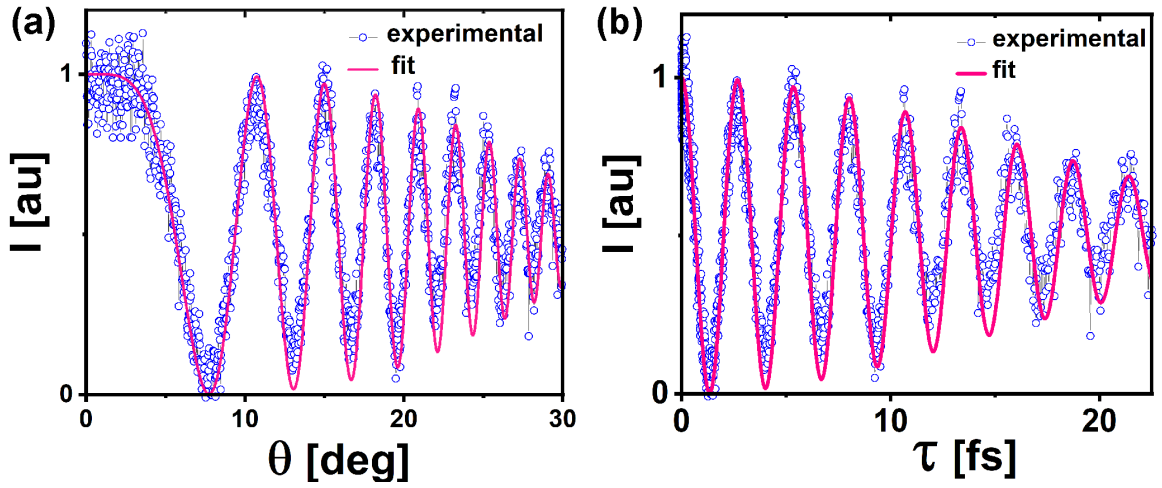

Figure 3.8: (a) Fs central fringe intensity (I) variation over a range of 30° rotation angle of glass plate and a theoretical fit curve (pink) corresponds to equation 3.8 in terms θ of are shown here. (b) I versus time delay (τ) after θ to τ calibration from equation 3.1 while theoretical fit (pink) curve corresponds to equation 3.8 in terms of τ.

3.5 Advantages of ultrathin delayline

3.5.1 Absolute zero delay reference

Absolute zero delay is the condition of exact overlap of two pulses in time domain. In the field of pump-probe spectroscopy, zero delay reference between the pump and probe pulse is crucial and is necessary for control and measurement of electron dynamics in attosecond time scale [25]. In order to achieve this condition, the delayline has to be nanometer scale controlled (0.3 nm corresponds to 1 *as* time) which is very difficult with commonly used piezoelectric based techniques due to its instability in position. There are indirect method available using multiphoton effects [65] or via atomic transitions [66] but are challenging to get the absolute zero delay reference

with them.

Measurement of fs pulses interferogram using ultrathin delay line gives a direct

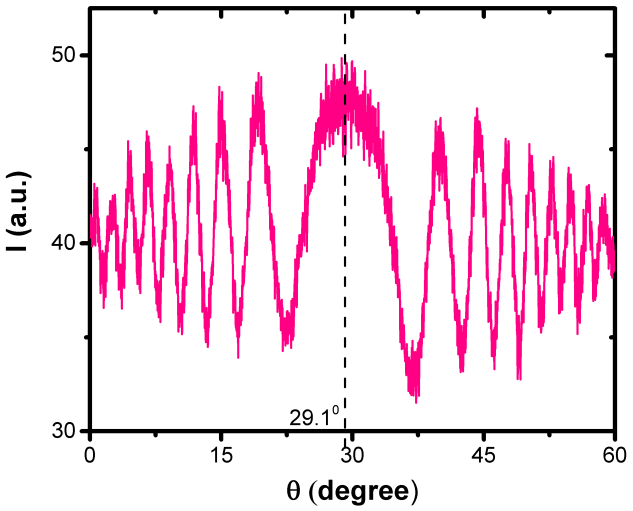

Figure 3.9: Interferogram with fs pulses showing zero delay reference position ($\theta = 29.1^0$) at the inversion symmetry point. Intensity fluctuations near zero delay point attributes to motor rotation and light intensity (detail in next section).

method of finding zero delay reference. Indeed, the parabolic dependence of τ over θ ensures zero delay position is not missed. A large angular deviation ($\theta \approx 7°$) is needed in order to become central maxima to become minima (Fig.3.8(a)). By overlapping back reflections of incident laser from both the glass plates on same Y-axis, our ultrathin glass plates are kept in a plane within 0.05° error. This time zero position is determined with a precision of 2.5 *as* corresponding to 0.05° (Fig.3.10).

Rotating the glass plate backward or forward from zero angle will always increase the OPD and hence a point of inversion symmetry can be found in interferogram as shown in Fig.3.9. The position of this inversion symmetry of interferogram is the zero delay position. At this position, both identical glass plates induce net zero path delay in parallel position. Similarly, this inversion symmetry will also help in determining the absolute zero time delay reference with intensity oscillations of generated high harmonics.

3.5.2 Attosecond resolution of delayline

Another advantage of this delay line is its attosecond resolution in delay steps. Most ultrafast measurements demand high resolution of attosecond in time domain to distinguish two different phenomena. In our delayline, the time delay (τ) induced vary quadratically with angle of rotation. Therefore, time resolution varies from nearly 2.5 *as* to few tens of attosecond *as* we go at higher angle with angular resolution of 0.05° as shown in Fig3.10.

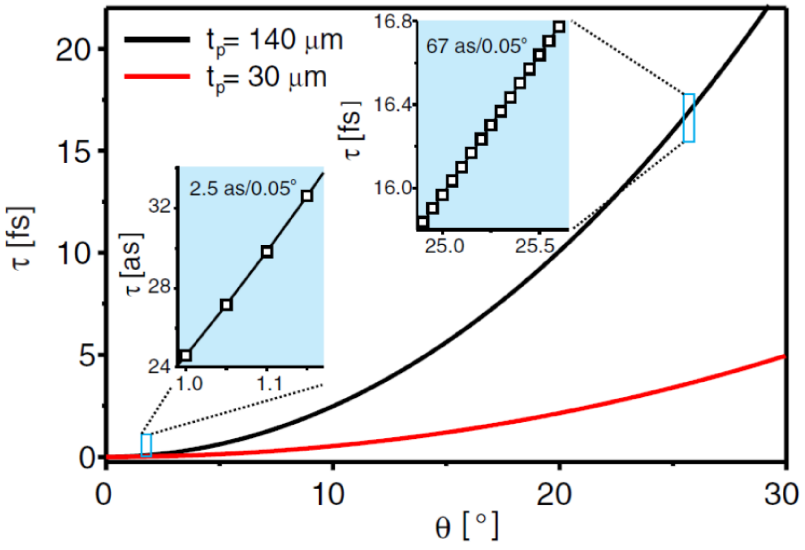

Figure 3.10: Time delay (τ) variation with angle of rotation θ for two different thicknesses of the glass plates. Inset: attosecond resolution near 1° and near 25° is shown for t = 140 μm glass plate.

Interestingly, resolution is very high of sub 1 *as* around zero angle due nonlinear behaviour of time delay. This resolution can further increased with a thinner glass plate (with 30 μm commercially available glass [61]) or lowering angular speed from 0.05°/s. The experimental measurement of OPD or time resolution is carried out using He-Ne laser interferogram. With θ to OPD conversion from self- calibration method, we obtained OPD resolution of around 300 pm corresponding to 1 *as* time delay in linear regime as shown in Fig.3.11. Here, bright to dark fringe tuning is done by rotating the glass plate with constant angular velocity of 0.5°/s which corresponds to OPD of $\lambda/2 = 316\ nm$. Due to nonlinear behaviour of OPD against θ, experimental data points are non uniformly distributed with higher density near zero OPD. Also, camera captured the laser intensity with around 30 fps that contributes to resolving the OPD further in this case.

In Fig.3.11, there are some small oscillations near zero OPD. We systematically tried to find the origin of these oscillations which are attributed to various noises the interferometer. These oscillations are mainly caused due to variation n instantaneous velocity of rotation motor (Fig.3.12). Also, there are small intensity fluctuations of He-Ne laser whose effect is seen largely near maxima/bright edge than the dark edge of the oscillation cycle. By using stable intensity lasers and better rotation stage, we can improve the noise-limited resolution of our delayline.

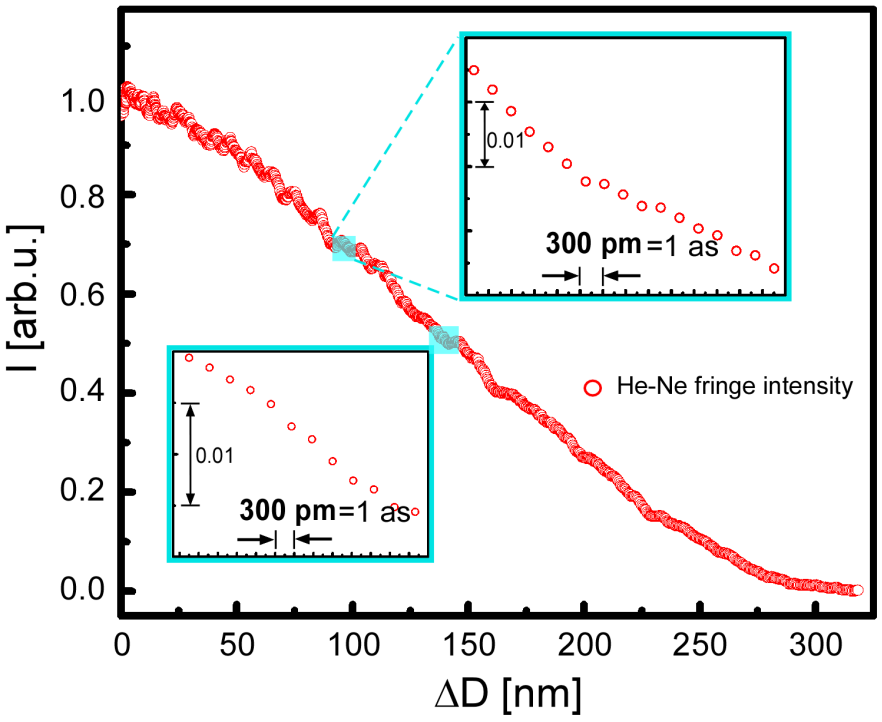

Figure 3.11: He-Ne laser intensity variation showing self calibrated picosale resolution in maxima to minima oscillation. Resolution of around 1 *as* (∼300 pm) is shown in linear regime with first cycle of He-Ne fringe intensity oscillation.

3.5.3 Stability of delayline

The stability of the delayline is a key feature for its application. Stability of the interferometer corresponds the fluctuation measurement in displacement or in time between the interferometric paths in the natural condition of our setup. It is calculated as root mean square (rms) value of relative path displacement over time. Mostly, fluctuations are caused due to intrinsic instability of interferometer's components and in the geometrical path of interferometer due to surrounding environment like air flow

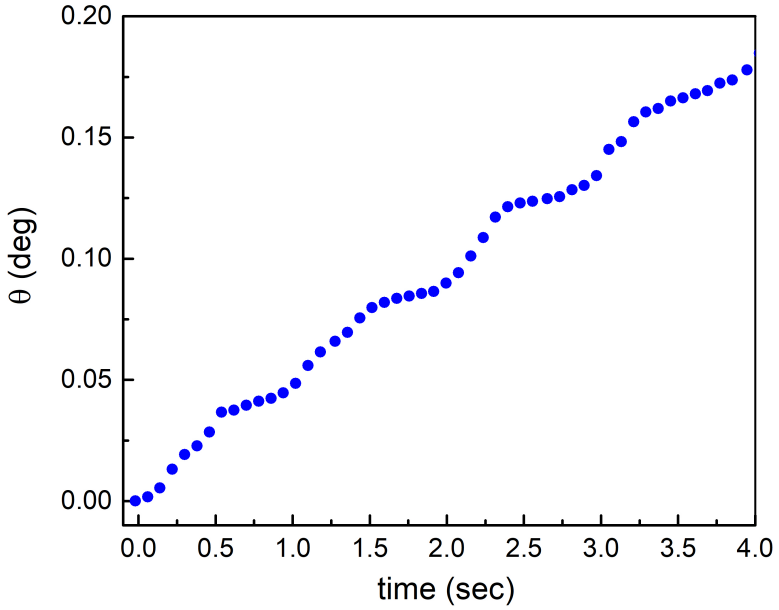

Figure 3.12: Experimental data showing angle variation in the motion of rotation motor (Thorlabs PRM1Z7). An oscillatory nonlinear behaviour is found suggesting small variation in instantaneous velocity that contributes in He-Ne intensity oscillations whereas average rotational velocity (0.05°/s) remains same.

or mechanical vibrations.

Since, we are not using any active stabilization technique, measurement of fringe fluctuation associated with our delayline becomes necessary. He-Ne fringes from ultrathin delayline are captured via a photodiode. In the beginning, we lower glass plate in order to calibrate intensity change in terms of wavelength or in time ($\lambda/2 \sim 1.05$ fs) and left the delayline for a long time without any external movement. Along that a small portion incident He-Ne laser beam is simultaneously measured from another photodiode. A similarity between fringe intensity and laser intensity is found with correlation factor of ~ 0.7 (Fig3.13 inset). This indicates that the main contribution of fringe intensity fluctuations of the ultrathin delay line comes from our He-Ne laser intensity and hence can be improved with an intensity stabilized laser. Our concern is to quantify our delayline stability rather than laser fluctuations. For that, we subtracted the laser caused fluctuation and resultant histogram shows about 2 *as* or 0.6 nm path stability (Fig.3.13). Such a good *as* stability is due to common interferometer path configuration of ultrathin delayline.

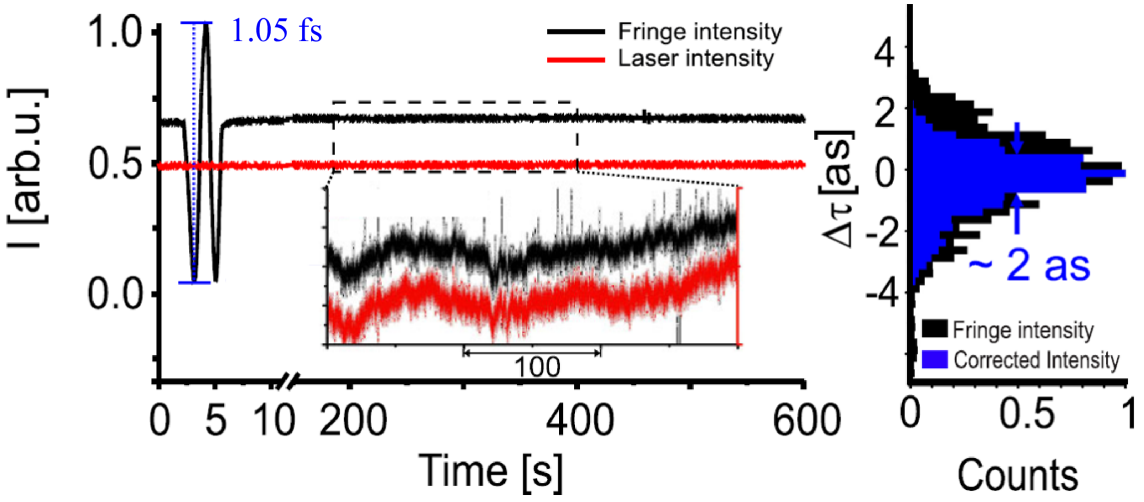

Figure 3.13: (a) Stability measurement of delayline using He-Ne laser. Initial oscillations in fringes intensity is used for calibrating intensity into time using self-calibration. Inset: Fringe intensity and laser intensity show similar trends of fluctuations. (b) Normalized histogram of delay fluctuations of fringe intensity data (black) and subtracted laser noise data from it (blue).

Limitations of ultrathin delayline

Although ultrathin delayine has a number of advantages, there are also a few limitations that should be discussed. One of the limitations is its applications for wide variety of ultrashort pulses. Its time delay range is 100 fs, therefore can not be used for similar or higher pulse duration measurement of ultrashort pulse. Though one chooses thicker glass but it will increase the dispersion effect drastically. Another is the lack of independent interferometeric paths in order to vary their properties like polarization.

3.6 Controlling yield of high harmonics with ultrathin delayline

The ultrathin delayline is tested for IR-IR delay in the process of high harmonic generation at our setup as shown in Fig.3.14. It has been placed before a plane mirror which hardly changed the beam alignment of our Attosetup.

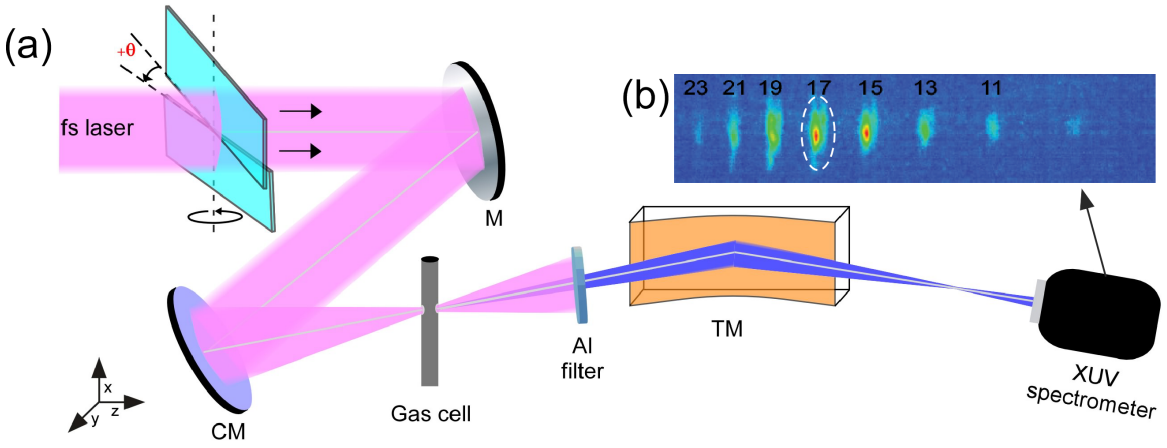

Figure 3.14: (a) Schematic of ultrathin delay line integration with attosecond beamline. The XUV spectrometer consists of a spherical grating and a micro-channel plate detector (MCP). M, plane mirror; CM, concave mirror; TM, toroidal mirror. (b) High harmonics spectrum with Argon gas observed on MCP detector. White dotted circle on H17 denotes the region of interest (ROI) for intensity tracking.

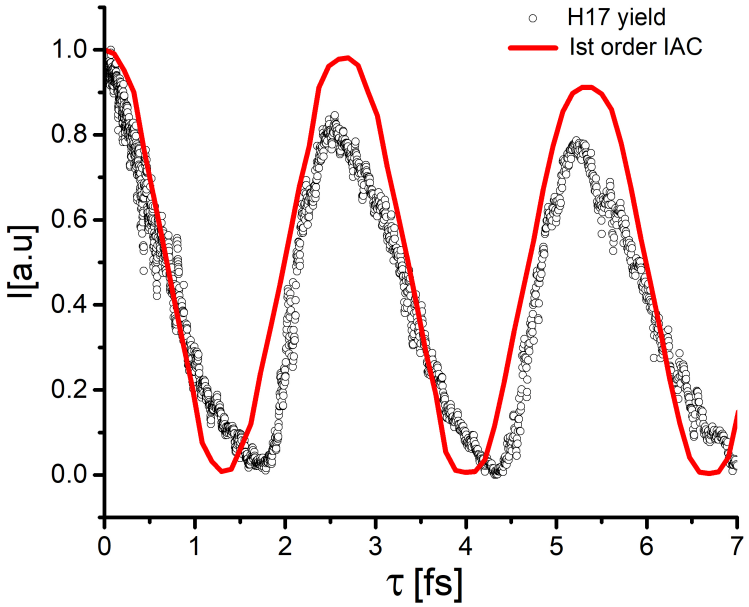

Figure 3.15: Variation of H17 yield with IR-IR delay which follows ist order interferometeric autocorrelation (IAC) of IR pulse of time period of around 2.7 fs.

The two IR beams (upper and lower parts) readily overlap in time domain and then time delay between them is controlled by precise rotation of glass plate. The generated

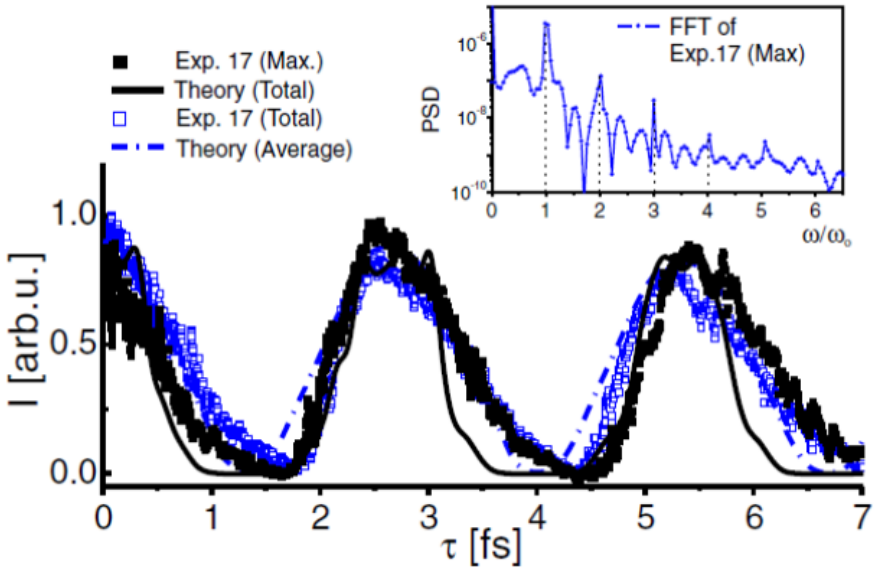

Figure 3.16: Variation in normalized yield of harmonic 17^{th} with IR-IR time delay is shown here along with theoretical result. Filled black square: maximum intensity by tracking a single central point of H17. Solid black line: total yield for the model atom. Empty square : Average intensity by tracking a ROI containing full H17. Dotted blue line: averaging of theoretical fit over half optical cycle. Inset: Fourier transform of H17 exp. (total) showing power spectral density (PSD).

XUV pulses from Argon gas are filtered out using Al filter and are captured using XUV spectrometer. The setup has been explained in detail in chapter 2.
The generated harmonics are video captured with time delayed IR pulses and analyzed. The harmonics are calibrated using transmission cutoff of an Al filter. Let's take highest yield Harmonic 17^{th} (H17). The yield or intensity (average intensity, circular ROI) of this harmonic is shown in Fig.3.15 which shows periodic oscillations of time period around 2.7 fs. The intensity oscillations follow IR fringe intensity variation or first order autocorrelation (AC) of IR pulses. Harmonic intensity oscillations are due to constructive and destructive interference of two fs beam paths having relative time delay between them. The fact that harmonics intensity oscillations obey similar time period of 2.7 fs validates the performance of delayline. Also, Fourier transform of H17 experimental intensity oscillations shows multiple peaks up to $4\omega_0$ which corresponds to $\sim$ 670 *as* (2.7/4 fs) as shown in Fig.3.16. This shows that the delayline has the capability of making attosecond resolution measurement.

We see that there is some asymmetry in H17 yield oscillations. We require HHG

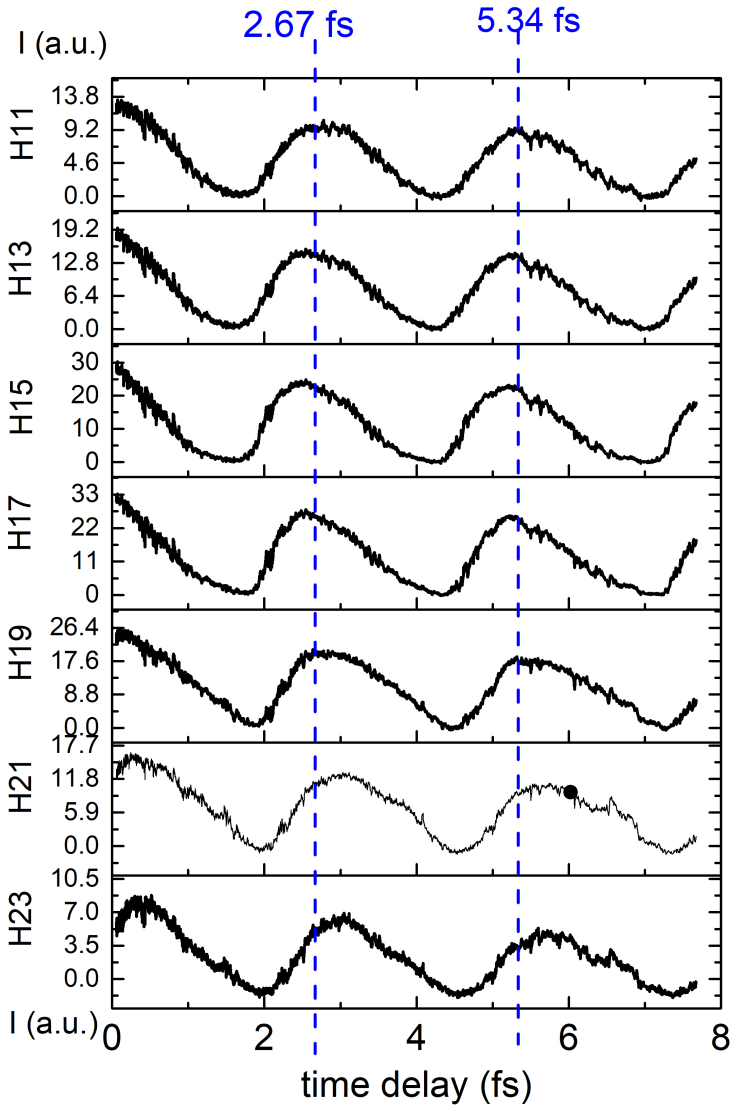

Figure 3.17: Periodic intensity (average) variation of all harmonics are shown here (stack form). Slight variation in phase delay between the oscillations of the harmonics with each other.

simulation in order to have better understanding. The theoretical simulation is then done by Dr. Ankur Mandal from our group and detailed explanation in out the scope of this thesis. The theoretical model is based on time dependent Schrodinger equation (TDSE) in 1D model and then numerically calculated Fourier transform of dipole acceleration [67]. The resultant theoretical H17 oscillations are shown in Fig.3.16. The theoretical data (theory(average)) is cycle-averaged (over T/2) in order to match focal volume averaging condition but does not completely match the experimental one. We

also checked the effect of CEP but could not make agreement with the experimental data. The mismatch between theory and experimental may be due to angular spread of the beam or propagation effect which is not included in 1D model.

We observed the yield modulation with slight asymmetry in all the harmonics and a slight phase delay between each harmonics (Fig.3.17). These features results from phase matching conditions need to be further explored in future. Though, our main task to check the performance of delayline with HHG is successfully completed.

3.7 Conclusion

In this chapter, we introduced a new compact ultrathin glass based delayline using wavefront division by a pair of micrometer thin glasses with negligible dispersion effects. Its design and development are reported here. This delayline has a number of advantages against the conventional delaylines used in ultrafast measurements. It is auto-aligned and in-line delayline (does not require change in beam path in order to place it) providing attosecond optical delay resolution. The delayline is self calibrated as shown in this chapter and provides attosecond stability of around 2 *as* measured experimentally. In the end, this delayline performance is validated by IR-IR delay control providing periodic variation in the yield of high order harmonics.
In future, a couple of things can be improved. One will be the use of 30 μm ultrathin glass that will give us temporal resolution even in zeptosecond domain. Other will be an experimental measurement of dispersion of the pulses using instruments or techniques like ellipsometer or white light interferometry, may help improve our analysis of dispersion with ultrathin delayline.

Chapter 4

Ultrashort pulse measurement with Ultrathin delayline

4.1 Introduction

Interferometric autocorrelation has become a widely used technique for ultrashort pulse metrology from few cycle femtosecond up to higher time scale [68–70]. Conventional autocorrelators based on Michelson and Mach-Zehnder interferometers are commonly used for such temporal measurements having thick glass beam splitters [71, 72]. Two or three photon absorption [73, 74] and second harmonic generation (SHG) in nonlinear crystals [75] are commonly employed for obtaining frequency resolved autocorrelation (FRAC) signal using these interferometers in order to measure ultrashort pulses. A schematic of commonly used FRAC technique is shown in Fig.4.1.

Such temporal measurements with ultrashort pulses require precise alignment, minimum distortion or dispersion in the measuring pulse, high temporal resolution of interferometer and high stability against external vibrations/fluctuations. To avoid dispersion, all reflective configurations such as Michelson type transmission grating, split mirror based delay line and reflective prism based delayline are reported earlier for long to few cycle femtosecond pulse metrology [76–81]. Most of them require specialized optics and complex setup for ultrafast pulse measurement. It becomes important as well as challenging to design an ultracompact, simple and highly stable dispersion balanced autocorrelator with easy alignment for recording of autocorrelation signal.

In this chapter, we use our ultrathin delayline which can act as a dispersion balanced

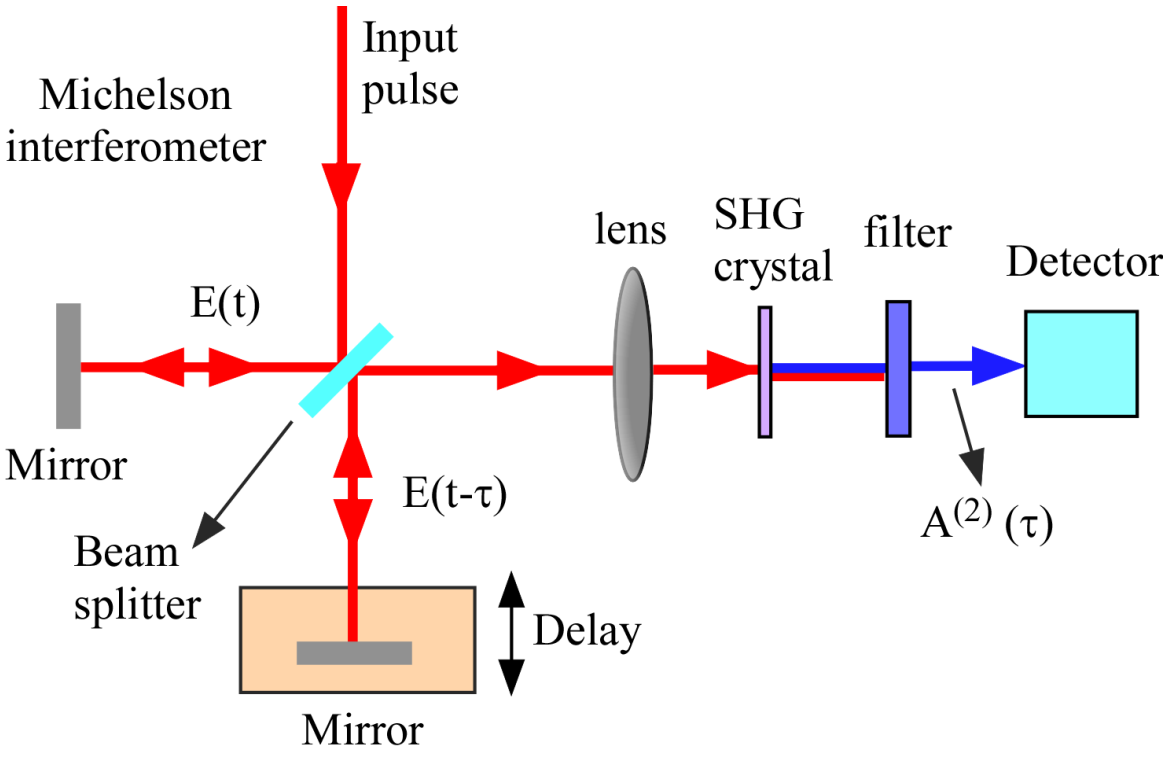

Figure 4.1: Schematic of FRAC setup using Michelson interferometer. The two time delayed pulses are focused on second harmonic generation (SHG) crystal and then SHG signal is measured with respect to time delay (τ) with a photodiode/camera as detector.

autocorrelator for fs pulse measurement (discussed in chapter 3). This autocorrelator is based on wavefront division of fundamental pulse having common path configuration to provide high stability and adds negligible dispersion in the measuring pulse. The autocorrelator is demonstrated with measurement of fs pulses from our amplifier part (femtosecond pulse generation system) via FRAC technique. The autocorrelator allows maximum throughput and provides high phase stability between replica beams due to ultra compact geometry. The present autocorrelator provides high temporal resolution of sub 10 attosecond which helps in better measurement. This autocorrelator is easy to align, compact, low cost and usable for a broad spectral range.

The mathematical expression of FRAC signal or 2^{nd} order interferometric autocorrelation (IAC) is written as [82],

$$IAC = A^{(2)}(\tau) = \int \left|[E(t-\tau) + E(t)]^2\right|^2 dt \tag{4.1}$$

$$A^{(2)}(\tau) = \int \left|E^2(t) + E^2(t-\tau) + 2E(t)E(t-\tau)\right|^2 dt$$

$$\begin{aligned} A^{(2)}\tau = & \int [I^2(t) + I^2(t-\tau)]dt \\ & + 4\int I(t)I(t-\tau)dt \\ & + 2\int [I(t) + I(t-\tau)]E(t)E^*(t-\tau)dt + c.c. \\ & + \int E^2(t)E^{*2}(t-\tau)dt + c.c., \end{aligned} \tag{4.2}$$

where E(t) = $E_0 e^{\iota\omega t+\phi}$ and E*(t) = $E_0 e^{-\iota\omega t+\phi}$. The other terms are $E(t-\tau) = E_0 e^{\iota\omega t-\tau+\phi}$ and I(t)=$\left|E^2(t)\right|$. Here, E(t) and $E(t-\tau)$ are electric fields corresponding to two interferometric paths. In expanded equation 4.2, the first term is constant while the second term denotes intensity autocorrelation. The third term oscillates with ω and fourth term oscillates with 2ω . The signal (IAC) has a unique property of having background/wings to peak ratio of 1:8 to validate the proper alignment of the autocorrelator [82].

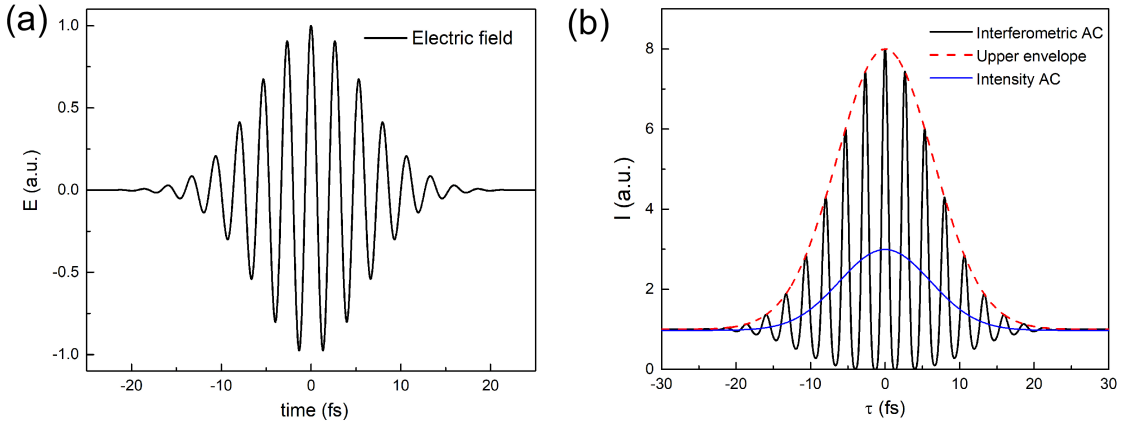

Figure 4.2: (a) Theoretical plot of electric field of a 10 fs (FWHM) Gaussian pulse. (b) Using equation 4.1, the corresponding interferometric autocorrelation (AC) signal showing background to peak ration 1:8. The intensity autocorrelation (blue) showing 1:3 i.e background to peak ratio.

4.2 Ultrathin autocorrelator setup

A schematic representation of ultrathin autocorrelator setup is shown in Fig. 4.3. The collimated near infrared (NIR) fs pulses of central wavelength ≈ 800 nm are to be characterized. The wavefront of fs pulses is symmetrically split via an identical pair of ultrathin glass plates having ∼ 140 μm thickness placed vertically with a gap which is less than or of the order of plate thickness.

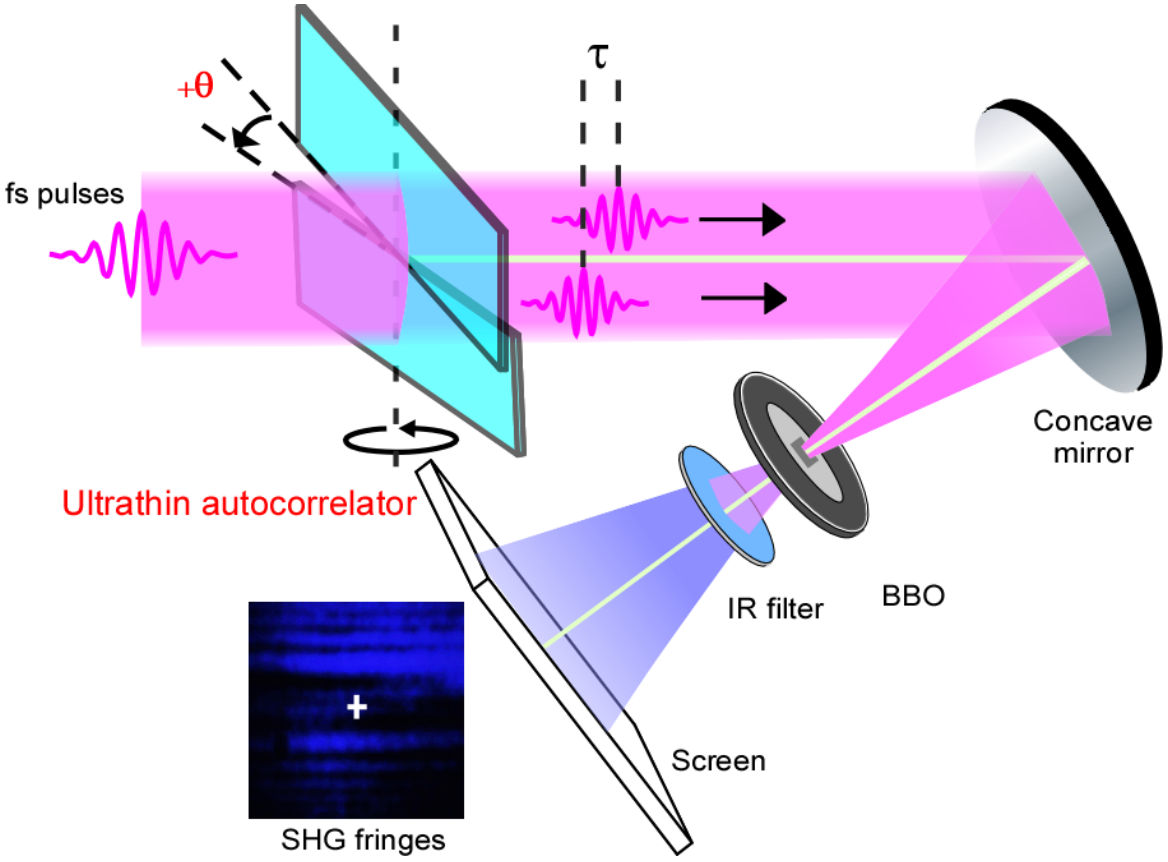

Figure 4.3: Schematic of FRAC measurement using ultrathin autocorrelator. The FRAC measurement has been taken via second harmonic intensity generated from BBO.

The pulse is incident normally on ultrathin interferometer and the two separated halves corresponding to upper and lower beams are time delayed (τ) with respect to each other by rotating the lower glass plate using a Thorlab's motorized stage (PRM1Z7). Rotation of glass plate induces an optical path delay due to refraction of light in the glass medium. These two halves which are replicas of each other, propagate in parallel geometry and are focused using a concave mirror (f = 10 cm) on

non-linear crystal medium such as BBO. The nonlinear 20 μm thick BBO (β-barium borate) crystal (cut angle = 28^0) having dimensions (2x2 mm) is placed at focal plane to generate second harmonics of incident IR pulse. A shot pass filter (FES700, Thorlabs) is placed after BBO to separate fundamental beam from generated blue part. The corresponding blue signal is observed on a white screen placed at a distance of 20 cm from the focus position and recorded using an ordinary camera.

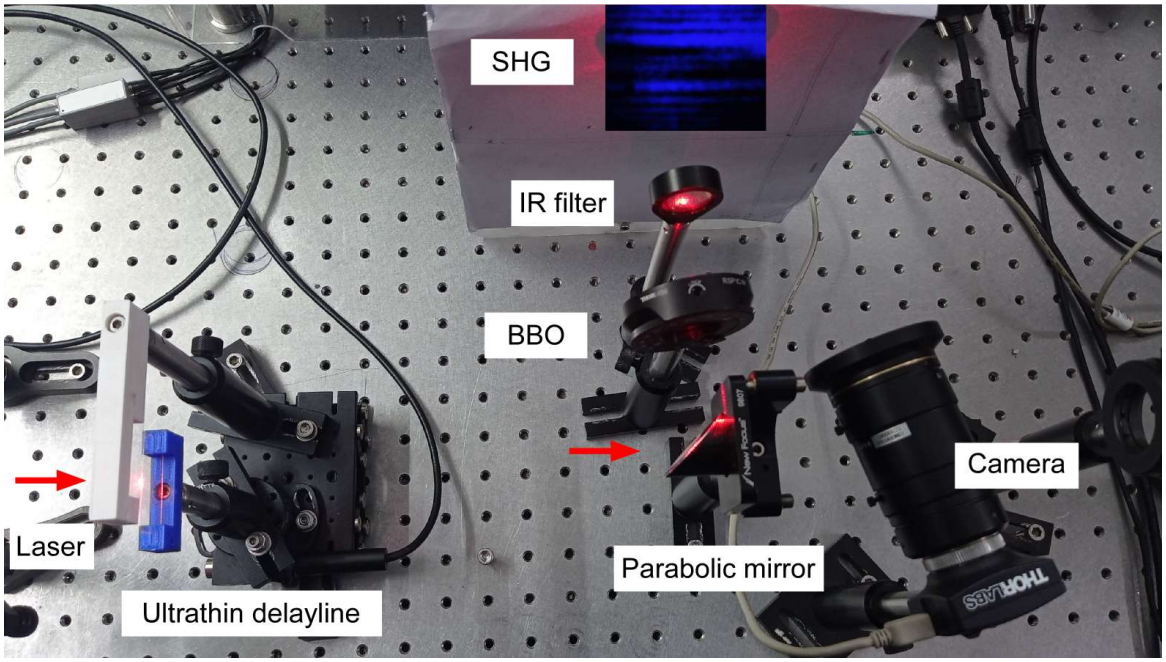

Figure 4.4: Picture of ultrathin glass based autocorrelator. Different components are labelled.

4.3 Measurement of sub 30 fs IR pulse

The second harmonics fringes are easily obtained with our ultrathin autocorrelator due to its geometry. The blue colour interference fringes are tracked and corresponding signal is obtained using setup in Fig.4.3. The lower glass plate is rotated with 0.2°/s angular velocity and the blue signal has been traced and calibrated angle into time delay between the two replicas of fs pulses using equation 3.1. The analyzed FRAC signal is shown in Fig. 4.5. The SHG is symmetrical and background to peak ratio is nearly approaching 1: 7.4 showing the good alignment of our ultrathin autocorrelator. Slight variation in the ratio may be due to quasi-colinear geometry of our delayline.

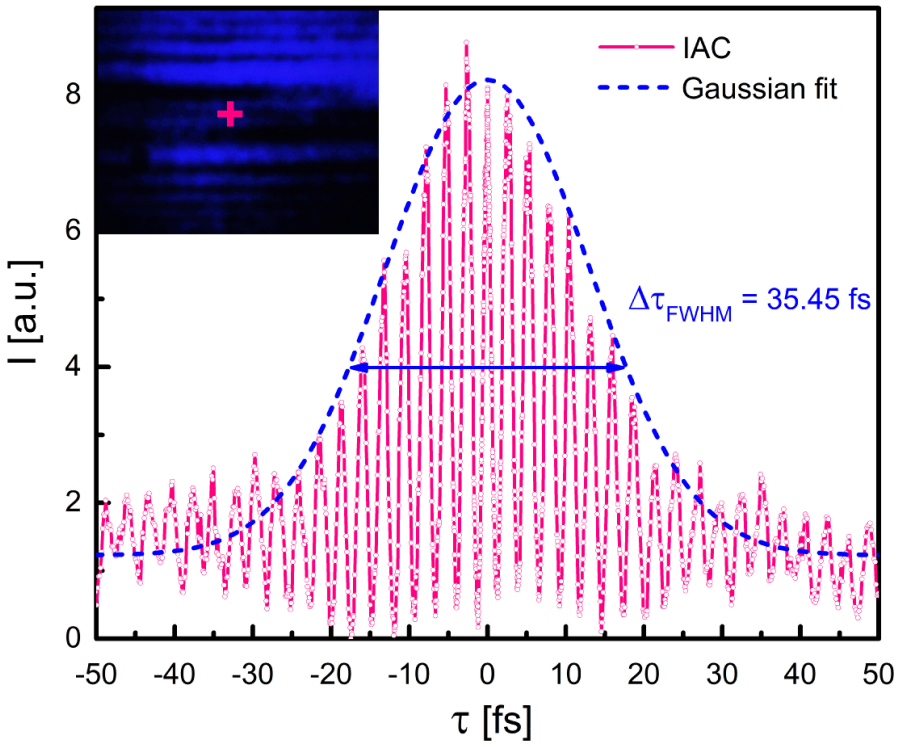

Figure 4.5: Experimentally obtained 2nd order intensity autocorrelation of fs pulses. The graph shows FWHM of 35.45 fs and corresponding pulse width of 25.14 fs (FWHM/$\sqrt{2}$). Inset: SHG blue color fringes and tracking point is shown here.

The central peak FWHM is calculated to be around 35.45 $\pm$ 0.03 fs which gives fs pulse width (FWHM/$\sqrt{2}$) of 25.14 $\pm$ 0.03 fs. The measured pulse width is within 1% error assuming 25 fs theoretical value. Here, $\sqrt{2}$ is de-convolution factor used for Gaussian shape pulses. This measurement validates the performance of the new ultrathin autocorrelator.

4.4 Conclusion

A compact autocorrelator realized with two vertically placed ultrathin glass slides acting as both split and delay unit, is demonstrated with femtosecond pulse measurement in near-IR regime through second harmonic generation via BBO. The autocorrelator offers negligible dispersion and shows high phase stability due to its common path configuration. This ultrathin autocorrelator accurately measures the fs pulses within 1% error.

Further, this autocorrelator can be used for even a few cycles i.e. sub-10 fs pulses due to its negligible pulse width broadening effect and high time delay resolution.

Chapter 5

Delayline as white light interferometer

5.1 Introduction

Interferometers are the popular optical techniques with which even a small measurement of distance of order of wavelength of light is possible. Usually, such small distance measurement is not achievable with other methods and thus it becomes an important tool in scientific meteorology. White light interferometers have a huge variety of applications such as surface topography via vertical scanning interferometry, thin film measurements, gravitational waves detection, characterizing coherence properties of optical sources etc [30–33, 36, 83].

An interferometer is commonly understood as an occurrence of interference phenomenon by superposition of two or more light paths which is further measured and analyzed. Optical interferometers are mainly divided into two categories, amplitude split and wavefront split of incident light. Michelson interferometer(MI), Mach-Zehnder and Mirau, are some of the examples of an amplitude split interferometer [38]. MI is the basic and commonly used interferometer in various optical measurements. It consists of a beam splitter, a reference mirror and an object mirror. The two paths of light beam reflected from reference mirror and object mirror are superimposed resulting in an interference pattern and its path difference is controlled by linear motion of the reference mirror [39]. A white light interferometer uses a broadband source of light like tungsten bulb. In this case, the path difference between reference mirror and object mirror must be within coherence length of the white light source (typically $<$ 5 μm) in order to obtain interference fringes.

However, it is hard to align an interferometer with such small path difference near

zero delay position with non precise linear translation stage. It is quite challenging to obtain repeatable auto reference to zero position through the above mentioned amplitude split interferometers. Here, the requirement of atleast nanometer scale OPD resolution is to be fulfilled by the interferometer. Also, mechanical vibration and acoustic noises associated with the setup make it hard for amplitude split interferometers to remain in stabilized form and results in fluctuations in white light fringe colours.

In order to obtain white light fringes in time efficient manner or obtain zero delay position easily, modifications in MI [84] and common path Sagnac interferometer [40] are reported earlier. Whereas wavefront split interferometers can replace amplitude split interferometers providing higher stability regarding path fluctuation due to their common path configuration geometry. But most wavefront split interferometers like Young's double slit, Fresnel biprism and Billet lens [41] show lack of OPD tunability and provide information about spatial coherence of light source only with the interference fringes [38]. A number of wavefront split interferometers based on split mirror or reflective prisms are reported which are commonly used with ultrafast pulses [85] but they can not readily produce white light fringes due to complexity in design and in beam alignment. So, a compact and simple wavefront split interferometer with tunable path length difference will be a good tool to be used in various white light interferometry applications.

For white light interferometers, optical component dispersion is crucial thing to compensate. Unbalanced dispersion in two interferometric paths can cause distortion in white light interferogram by producing asymmetry in interferogram or increment in its FWHM [34, 86]. It is important to balance the dispersion in order to have quantitative measurements in white light interferometry. Also, dispersion will lead to difficulty in obtaining zero delay position commonly faced in conventional designs of white light interferometers. The zero path delay position is usually estimated with envelope's amplitude method in white light interferograms [87].

In order to obtain white light fringes readily, we use our ultrathin delayline as a white light wavefront split interferometer. We used ultrathin glass plates in our interferometer. It is ultrastable to path fluctuations and does not need precise beam alignment. Also, it is capable of providing picoscale resolution in the measurement of white light interferograms. This setup directly gives white light fringes due to zero path position in parallel configuration of the glass plates. Also, its optical path difference is controlled by precise rotation of one of the glass plate. Further, this white light

interferometer is demonstrated for measurement of the coherence length of various broadband sources.

5.2 White light interferometer setup

The schematic of ultrathin delayline used a white light interferometer is shown in Fig5.1. Most of the components used here are common to white light MI except beam splitter and detector. In the schematic, the variable slit (s) is used to make white light spatially coherent [88, 89] necessary to obtain white light fringes and we will discuss it in detail in next section. Using a collimator lens (L1), white light is directly incident on ultrathin interferometer. An aperture is used to control intensity of white light on camera chip to avoid over-illumination. The setup consists of a convex lens (25cm) to overlap the two interferometric paths at CCD camera chip (Thorlabs DCC1645C) placed near the focal plane. The white light fringes are observed in very narrow region and need a camera chip providing higher angular resolution than our naked eye to observe and analyze these fringes. Our lens-camera system has an angular resolution (pixel width/f) of around 16 μrad (1 pixel size of camera $= 4 \times 4\ \mu m^2$ and focal length of lens = 25 cm) whereas our eye has resolution of around 300 μrad [90].

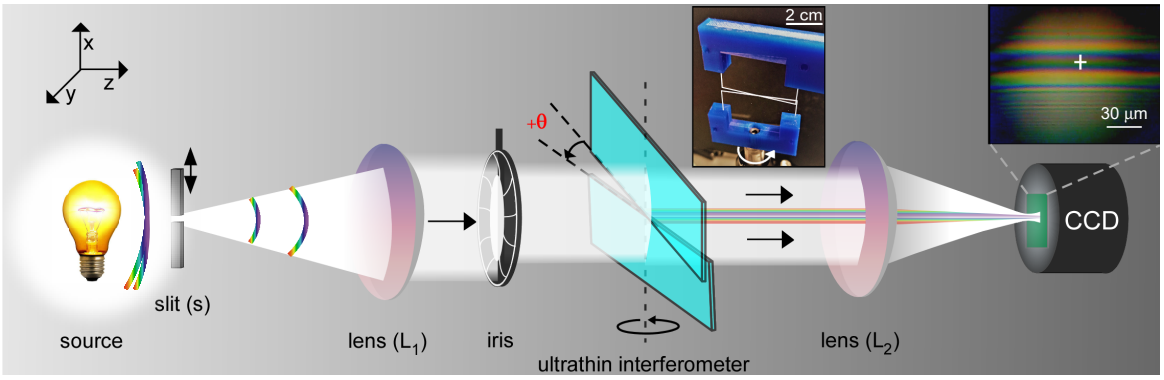

Figure 5.1: A schematic diagram of ultrathin white light interferometer. A broadband light source is made incident on interferometer after passing through a variable slit (s) and collimator lens (L1). The white light interference fringes are collected on a camera chip with a convex lens (L2). Insets: Pictures of the interferometer and a white LED source interference fringes.

In ultrathin white light interferometer, the two exactly same glass plates in parallel position directly result in formation of white light fringes. This interferometer is very time efficient regarding white light fringes observation without any tedious

alignment practice as in conventional Michelson interferometer. Also, the parallel position of both glass plates ensures the zero path delay position (ZPD). The ZPD is the condition at which all the wavelengths/wavenumbers of light source contribute to interferogram giving maximum intensity at that point (Fig.5.2). All the spectral components interfere constructively at ZPD.

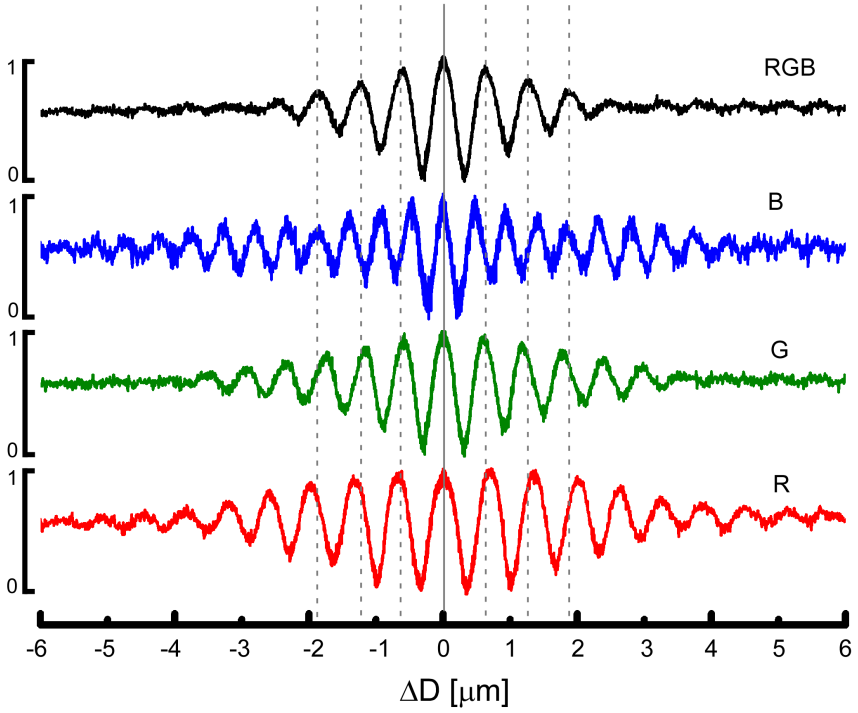

Figure 5.2: Experimental white light interferogram (RGB) along with its R, G and B components. All spectral components (R, G, B) interfere constructively (in phase) at zero path difference position.

The rotation of lower glass plate in ultrathin interferometer provides required optical path difference for having a white light interferogram as discussed in chapter 3. The range of OPD is zero to 32 μm for $\theta_{max} = 60^{\circ}$ which is sufficient to estimate the coherence length of most broadband sources. A sample of white light fringes of white LED source is shown in Fig.5.1, whose outer part is due to slit diffraction and remains constant upon rotation while middle part shows interference colored fringes. The diffracted part from each glass plate edge partially overlaps in the central region resulting in interference fringes. The colour of central fringe changed deterministically with OPD change. Note that any axial chromatic aberration from the focusing lens adds only a static background colour and does not change with OPD variation.
The ultrathin glass plates (t= 140 μm) induce group delay dispersion (GDD) $\sim$ 10 fs^2

(estimated in section 2, chapter 3) while same material glass beam splitter (BS, t= 5 mm) will induce GDD $\sim$ 1000 fs^2 commonly used Michelson interferometer (white light passes 3 times through BS). These calculations show negligible dispersion compared to conventional interferometer and whatever dispersion these ultrathin glasses induce, it is identical for both the interferometric arms making it a balanced interferometer. A balanced interferometer means that its path lengths in both the arms are equal for all frequencies.

5.3 Measurement of coherence length of various light sources

There are two types of coherence associated with a light source i.e. temporal coherence and spatial coherence. A laser is highly spatial coherent light source but may have high temporal coherence (e.g. He-Ne laser) or low temporal coherence (e.g. fs pulse beam).

5.3.1 Temporal coherence

Temporal coherence length ($L_c = c \times t_c$) is one of the characteristic property of a light source. Coherence time (t_c) is calculated as inversely proportional to spectral bandwidth ($\Delta\nu$) of the light source. Temporal coherence denotes the phase correlation of the waves at a particular point in space at different instants of time [38]. High temporal coherent light is related to its monochromatic nature. The temporal coherence length can be calculated assuming a Gaussian spectrum of light [91] as

$$L_c = \sqrt{\frac{2\ln 2}{\pi}} \frac{\lambda_0^2}{\Delta\lambda} \tag{5.1}$$

where λ_0 is central wavelength of light source and $\Delta\lambda$ is spectrum bandwidth (FWHM). It can also be measured from the interferogram of light source in which coherence length is defined as the OPD at which intensity value or visibility becomes 1/e of its maximum intensity value [86, 92].

Most of the white light sources have low temporal coherence of order of a few micrometer and its measurement demands nanometer control and stability in OPD which is provided by the ultrathin interferometer. Different white light sources such as tungsten bulb and white LED are used in this setup (Fig.5.1) and their corresponding fringes are observed as shown in Fig.5.3. The interference fringes of different light

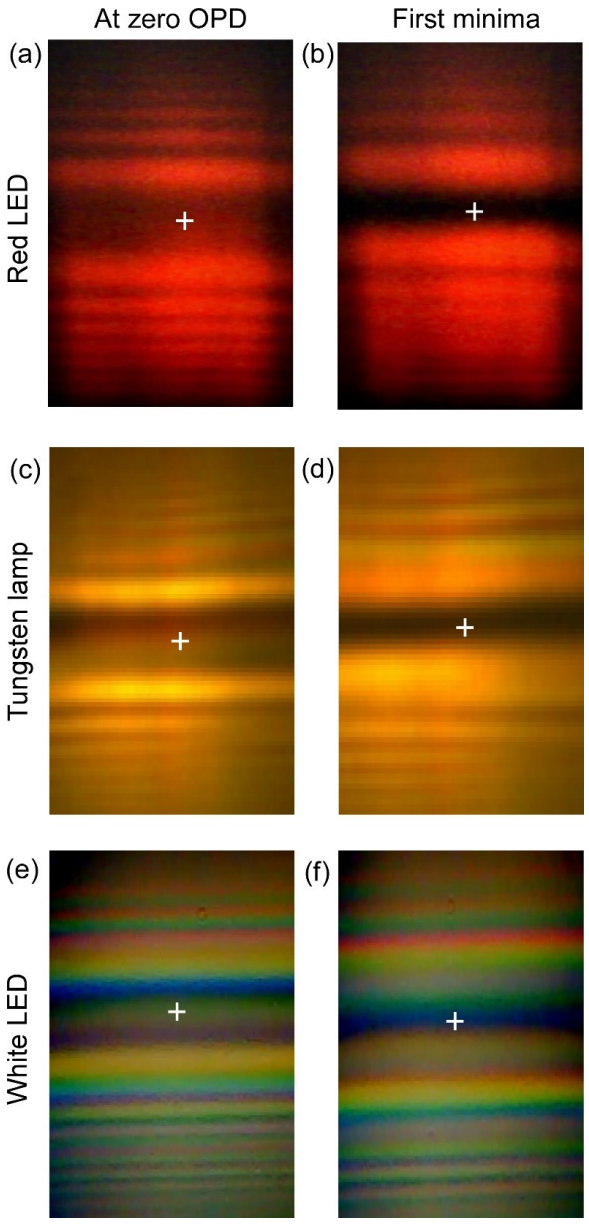

Figure 5.3: Images of red LED, tungsten and white LED source fringes captured at CCD chip using ultrathin glass interferometer, showing constructive interference (maxima) at zero OPD and destructive interference (first minima). The cross mark shows the intensity tracking position for interferogram.

sources in the central region will evolve with OPD change. Here, the lower glass plate is rotated with angular speed of 0.5°/s and obtained the interferogram upon angle to OPD conversion using equation 3.7. Here, the previously performed calibration with He-Ne laser is still valid for broadband white light sources [35].

We also used a red LED light source having a Gaussian shaped spectrum in order

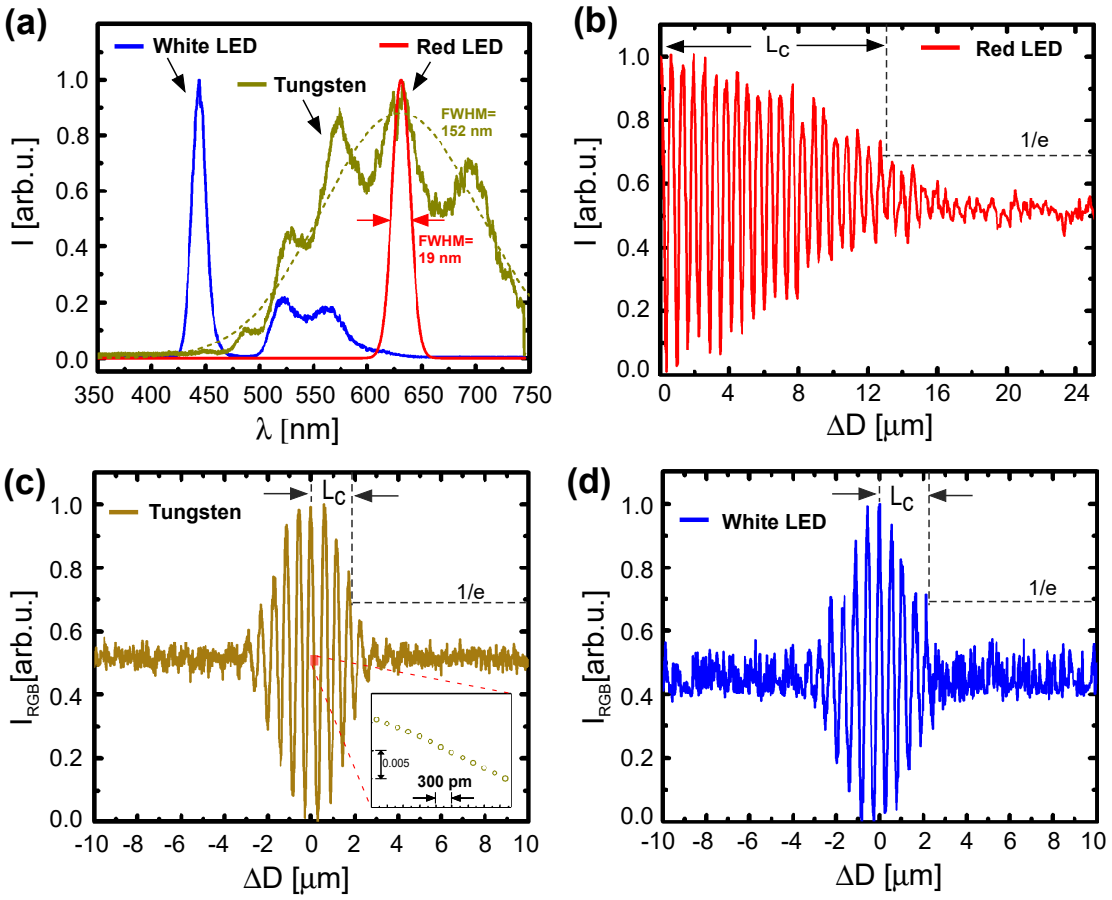

Figure 5.4: (a) Measured spectra of three different light sources using Thorlabs spectrometer (CCS100). Experimental interferogram of (b) red LED, (c) tungsten bulb and (d) white LED. The corresponding coherence length L_c is the OPD corresponding to 1/e of peak value is labeled. Inset in (c) shows picoscale resolution in the measurement.

to validate our experimental measurement of coherence length approach for our interferometer. The spectrum of red LED is measured via a spectrometer (Thorlabs, CCS100) and corresponding central $\lambda_0 = 631\ nm$ and FWHM bandwidth $\Delta\lambda = 19\ nm$ are measured (Fig.5.4(a)). Using these parameters, theoretical coherence length $L_c = 13.86\ \mu m$ is calculated from equation 5.1. With red LED interferogram, we measured the experimental value $L_c = 13.02 \pm 0.04\ \mu m$ which is in good agreement with the theoretical estimate within 6% error (Fig.5.4(b)).

We measured spectrum of tungsten bulb and white LED light source as shown in

Fig.5.4(a). The oscillations in tungsten spectrum may be due to etalon effect in spectrometer [93]. In Fig.5.4(c) of the tungsten bulb interferograms, $L_c = 1.92 \pm 0.029$ μm is measured which was also in reasonable agreement with the theoretical estimate of 1.75 μm calculated. This theoretical calculation is done by fitting a Gaussian function to tungsten spectrum as shown in Fig. 5.4(a) and used fit curve central parameters. The inset in Fig.5.4(c) also shows a picoscale resolution of around 300 pm with ultrathin interferometer that helps in precise measurements with these broadband interferograms.
Similarly, experimental coherence length of white LED source is found to be 2.22 $\pm$ 0.035 μm (Fig.5.4(d)). Here, we see the baseline noise in broadband sources interferograms which is caused mainly by intrinsic intensity fluctuations of these broadband light sources. A small discrepancy between theoretical and experimental values may be due to non-Gaussian emission spectra of these sources as shown in fig.5.4(a).

5.3.2 Spatial coherence

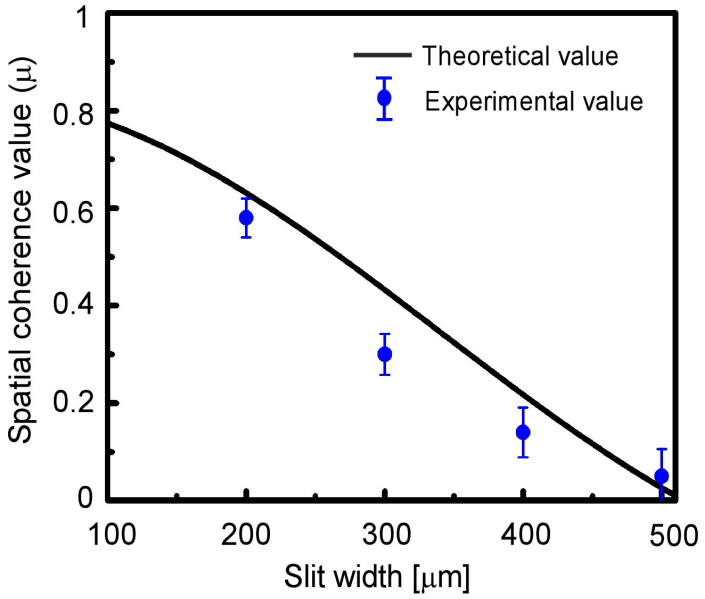

Figure 5.5: The effect of slit width (s) on spatial coherence value (μ) or visibility (V) of fringes of white LED source. Theoretical curve corresponds to $A\left|\sin(\frac{\pi us}{\lambda L})/(\frac{\pi us}{\lambda L})\right|$ with experimental parameters u= 250 μm, λ= 440 nm, L= 32 cm and A= 0.83.

Spatial coherence denotes the phase correlation between the electric fields at two different points on a single wavefront transverse to direction of beam propagation. It tells us about how much uniform the phase of light wavefront is. It can be measured

via a young's double slit setup and contrast of the fringes will directly provide the spatial coherence value (μ) of the source [88].

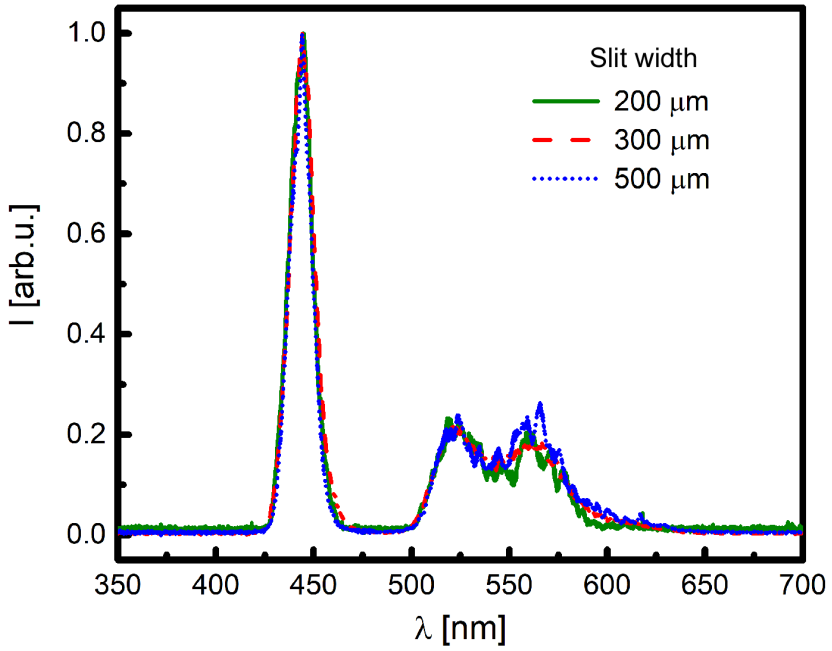

Figure 5.6: Spectrum of white LED with variation of slit width is shown here. Spectrum is normalized to unity (for maximum intensity peak around 450 nm) for each slit width.

For our setup, spatial coherence value (μ) mathematical expression can be written as [38],

$$\mu = \left|\sin(\frac{\pi us}{\lambda L})/(\frac{\pi us}{\lambda L})\right| \tag{5.2}$$

where u is central gap between two glass plates, s is slit width, λ is central wavelength of light used and L is distance between slit and interferometer. It is directly evident that μ will increase by narrowing the slit width (s) or increasing the distance L.

In Fig.5.1, we used a rectangular micro-slit of length 1 cm and variable width (s) from 200 μm to 500 μm. It has sharp edges in order to make nearly a single point source of light. It helps us in changing incoherent white light into partially spatial coherent as previously reported [88, 89]. The purpose of this slit is to control the contrast of the fringes in order to observe white light fringes cleanly. It has no effect on temporal coherence of light source as it does not vary spectrum of the light source as shown in Fig.5.6.

The experimental measurement of the spatial coherence value μ of white LED source

at different slit widths is done in our setup. We measured the visibility (V) of the interferogram at each slit width, as shown in Fig.5.5. The visibility (V) can be defined as,

$$V = \frac{I_{max} - I_{min}}{I_{max} + I_{min}}. \tag{5.3}$$

In Fig.5.5, the experimental values show good agreement with theoretical curve. We measured temporal coherence measurement with s = 200 μm to obtain maximum contrast in our setup. The central gap between the glass plates is also kept minimum (u $\sim$ 140 μm) to get high contrast. However, light transmitted through this central gap will not interfere (due to small temporal coherence length of white light source) with two paths corresponding to upper and lower glass plates and adding a background light only.

5.4 Modifications in WLI interferometer

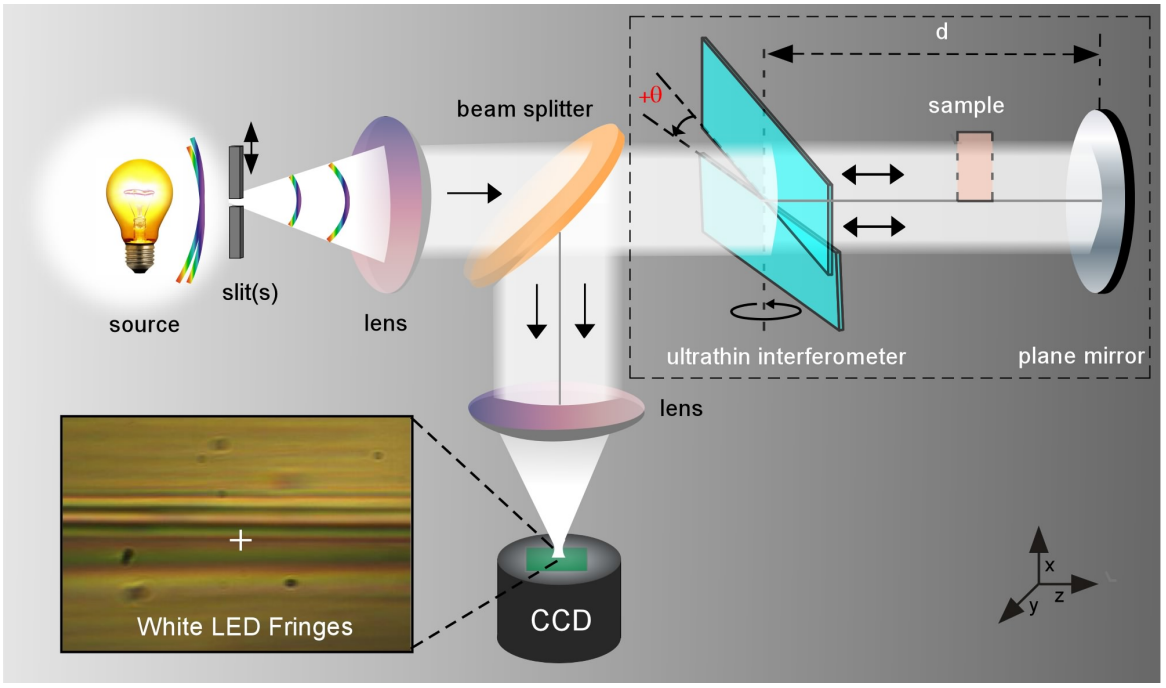

Figure 5.7: Schematic of double pass ultrathin interferometer. Inset: white LED interference fringes are shown.

A double pass white light interferometer is developed as shown in Fig.5.7. The previous white light interferometer is modified in order to make cavity based measurements. Tungsten interference fringes are also formed with this setup. One advantage of this setup is zero lateral shift in this geometry if we use thick glass plates. Here, lateral shift is compensated due to back and forth travel of light with same path. In this configuration, the rotation of the glass plate will induce double the optical path delay (OPD) for same angle of rotation compared to our previous geometry.

5.5 Conclusion

A new wavefront split based tunable white light interferometer is demonstrated which can be used for multiple applications in white light interferometry. This interferometer is compact, robust, dispersion balanced and easy to align which readily forms white light fringes. The zero path difference position is directly obtained by aligning the two glass plates in parallel position. It provides picometer scale tunability in OPD by rotating the ultrathin glass plates precisely.
The ultrathin interferometer is used for measurement of temporal coherence length of a few microns of different broadband white light sources. It is also be used for spatial coherence information of white LED source. This white light interferometer has huge potential to use in many applications like in measurement of optical properties of biological thin films and solutions replacing the Rayleigh interferometer [94] or optical density fluctuation of air due to humidity, turbulence and temperature [38]. Further, it can be used in most white light interferometry applications.

Chapter 6

General Conclusions and Future Perspectives

In this thesis, the following objectives are achieved.

- Developed and optimized a table-top coherent XUV pulse source via high harmonic generation (HHG) in gas medium. Harmonics optimization and characterization are performed to get better reproducibility.
- Designed and developed a new delayline having features like absolute zero delay reference, attosecond delay resolution and stability. It is experimentally realized in controlling the yield of high harmonics and attosecond time scale measurement.
- A dispersion free autocorrelator using ultrathin delayline is demonstrated with characterization of fs pulses in time domain using FRAC technique.
- A picometer tunable white light interferometer is demonstrated with temporal and spatial coherence measurements of various broadband sources of light.

The thesis consists of development and optimization of a table top high harmonics attosecond source and different applications of a new delayline in HHG, in characterization of fs pulses and in white light interferometry are demonstrated.

At first, we developed a reproducible attosecond pulse generation setup via high harmonic generation phenomenon with fs IR pulses. The characterization and optimization of harmonics has been done which is an important goal to make our ATTO-setup ready to use facility.

We designed and realized a new ultrathin delayline for time resolved experiments. This ultrathin delayline with sub 10 *as* resolution and around 2 *as* stability provide a unique feature of time zero delay reference which is beneficial in ultrafast experiments. Then it is used for controlling the yield of high order harmonics via IR-IR time delay of input fs pulses. Harmonics yield contains sub cycle oscillations, thus making this delayline capable of attosecond resolved measurement. Our work regarding this ultrathin delayline having tremendous resolution and stability will help in resolving attosecond dynamics in different systems such as photoionization of atomic and molecular gas and in photonic streaking phenomenon with gas or solids.

Two applications of ultrathin delayline are also demonstrated in the thesis. First, a dispersion and alignment free ultrathin autocorrelator for measuring fs pulse in time domain. A second application is a tunable wavefront split ultrathin white light interferometer for measuring the temporal coherence length of various broadband sources like tungsten and white LED with picometer resolution. Further, a double pass configuration of this white light interferometer having a sample cavity is also proposed for additional applications in probing dynamical properties of matter and in existing applications of white light interferometry.

In future, using ultrathin delayline for XUV-IR delay is an important step. With these advancements, we will be able to carry out attosecond pulse characterization using RABBIT or photonic streaking. Further, this delayline can be used for attosecond resolved measurements in various ultrafast techniques such as photoionization of atomic and molecular gas or transient absorption spectroscopy.

Appendix A

Mathematical background of optical path delay with rotation of glass plate

Derivation of time delay equation

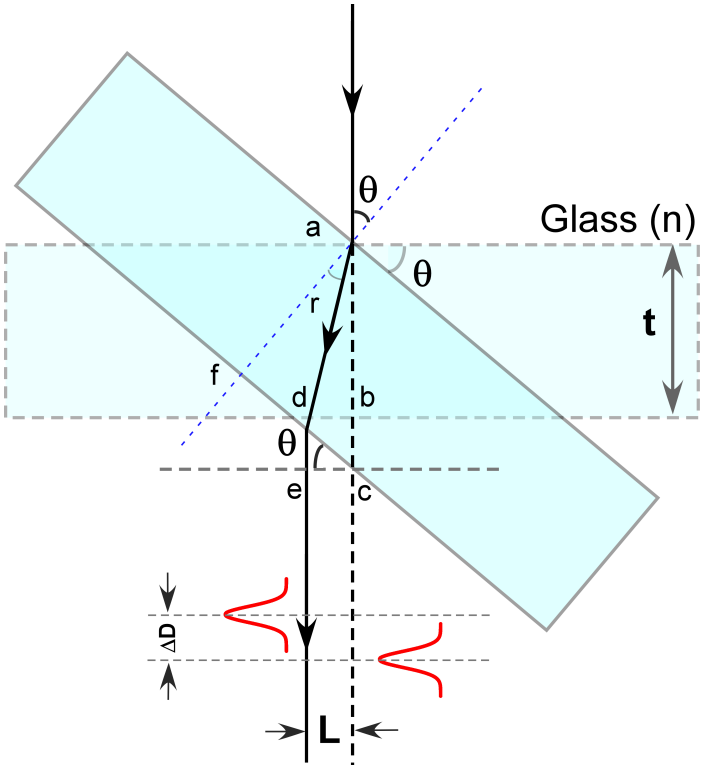

Figure A.1: Schematic showing optical path difference (ΔD) and lateral shift (L) by rotating glass plate to angle θ. t,thickness of glass plate; n, refractive index ; r, refraction angle.

The optical path difference (ΔD) when a glass is rotated by a angle θ, is written (from FigureA.1) as;

$$\Delta D = (n\overline{ad} + \overline{de}) - (n\overline{ab} + \overline{bc}) \tag{A.1}$$

In Δ afd; $ad = \frac{t}{\cos r}$.
Also, in Δ dec; $\frac{de}{dc} = \sin\theta$. On solving further,

$$de = dc \sin\theta \tag{A.2}$$

$$= (fc - fd)\sin\theta. \tag{A.3}$$

From Δ afc and Δ afd;

$$de = (t\tan\theta - t\tan r)\sin\theta \tag{A.4}$$

From FigureA.1, ab =t and bc = ac-t .
By putting value of ac from Δ afc, we get bc = $\frac{t}{\cos\theta} - t$.
Also, from law of refraction (air-glass interface);

$$\sin\theta = n\sin r \tag{A.5}$$

By inserting above all in equation A.1, we obtained equation similar to reference [20].

$$\Delta D = \frac{nt}{\cos r} + t\sin\theta(\tan\theta - \tan r) - nt - t(\frac{1}{\cos\theta} - 1) \tag{A.6}$$

$$= nt(\frac{1}{\cos r} - 1) + t[(\tan\theta - \tan r)\sin\theta - (\frac{1}{\cos\theta} - 1)]. \tag{A.7}$$

Further solving in simpler form;

$$\Delta D = \frac{nt}{\cos r} - nt + t[\frac{\sin^2\theta}{\cos\theta} - \frac{\sin r \sin\theta}{\cos r} - \frac{1}{\cos\theta} + 1] \tag{A.8}$$

$$= \frac{nt}{\cos r} + \frac{t\sin^2\theta}{\cos\theta} - \frac{t\sin r\sin\theta}{\cos r} - \frac{t}{\cos\theta} - (n-1)t \tag{A.9}$$

$$= \frac{-t}{\cos\theta}(1-\sin^2\theta) + \frac{t}{\cos r}[n - \sin r\sin\theta] - (n-1)t \tag{A.10}$$

$$= -t\cos\theta + \frac{t}{\cos r}(n - \frac{\sin^2\theta}{n}) - (n-1)t \tag{A.11}$$

$$= \frac{t}{n\cos r}(n^2 - \sin^2\theta) - t\cos\theta - (n-1)t \tag{A.12}$$

$$= \frac{n^2t - t\sin^2\theta - nt\cos\theta\cos r}{n\cos r} - (n-1)t \tag{A.13}$$

$$= \frac{n^2t - t\sin^2\theta - nt\cos\theta\sqrt{1-\frac{\sin^2\theta}{n^2}}}{n\sqrt{1-\frac{\sin^2\theta}{n^2}}} - (n-1)t. \tag{A.14}$$

Optical path difference can be written in this form which is similar to reference [2].

$$\Delta D = \frac{n^2t - t\sin^2\theta - t\cos\theta\sqrt{n^2-\sin^2\theta}}{\sqrt{n^2-\sin^2\theta}} - (n-1)t \tag{A.15}$$

For simplification, put $f(\theta) = \sqrt{n^2-\sin^2\theta}$

$$\Delta D = \frac{t[n^2 - \sin^2\theta - \cos\theta f(\theta)]}{f(\theta)} - (n-1)t \tag{A.16}$$

$$= t[f(\theta) - \cos\theta] - (n-1)t \tag{A.17}$$

Time delay $(\Delta\tau) = \frac{\Delta D}{c}$ where c is the speed of light in air.

$$\Delta\tau = \frac{t}{c}[f(\theta) - \cos\theta - (n-1)]. \tag{A.18}$$

Lateral shift expression

From FigureA.1, Lateral shift (L) is written as;

$$L = \overline{ec} = \overline{dc}\cos\theta \tag{A.19}$$

$$= (t\tan\theta - t\tan r)\cos\theta \tag{A.20}$$

$$= t[\sin\theta - \frac{\sin r\cos\theta}{\cos r}] \tag{A.21}$$

$$= \frac{t[\sin\theta\cos r - \sin r\cos\theta]}{\cos r} \tag{A.22}$$

$$= \frac{t[\sin\theta\sqrt{1-\frac{\sin^2\theta}{n^2}} - \frac{\sin\theta}{n}.\cos\theta]}{\sqrt{1-\frac{\sin^2\theta}{n^2}}} \tag{A.23}$$

$$= \frac{t[\sin\theta\sqrt{n^2-\sin^2\theta} - \frac{\sin 2\theta}{2}]}{\sqrt{n^2-\sin^2\theta}} \tag{A.24}$$

$$= t\sin\theta - \frac{t\sin 2\theta}{2f(\theta)} \tag{A.25}$$

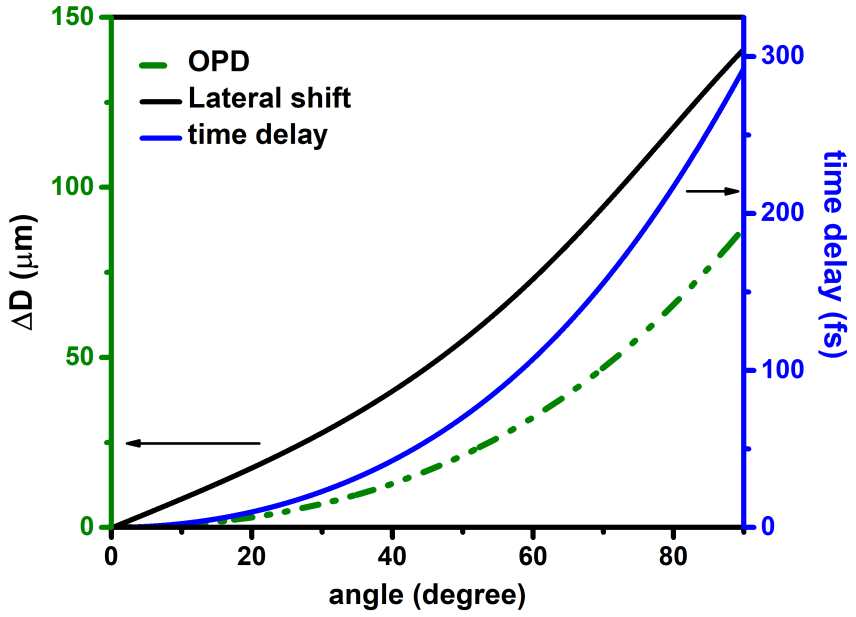

Figure A.2: Theoretical plot of OPD, relative time delay and lateral shift as a function of rotation angle (θ). Here, n is taken as 1.52 and t is taken as 140 μm.

Taylor series expansion

Optical path delay equation can be written explicitly as a function of θ for small angle by using Taylor series expansion [95].

$$\Delta D(\theta) = \Delta D(0) + \Delta D'(0)\theta + \frac{1}{2!}\Delta D''(0)\theta^2 + \frac{1}{3!}\Delta D'''(0)\theta^3 + ... \tag{A.26}$$

We have a derived simple expression for optical path delay where $f(\theta) = \sqrt{n^2 - \sin^2\theta}$,

$$\Delta D(\theta) = t[f(\theta) - \cos\theta] - (n-1)t. \tag{A.27}$$

Upon solving above equation (obtained derivatives using Mathematica), odd powers of θ get vanish and we get

$$\Delta D(\theta) = \frac{(n-1)t}{2n}\theta^2 + \frac{(4n^2 - n^3 - 3)t}{24n^3}\theta^4 + ... \tag{A.28}$$

and corresponding time delay is;

$$\Delta\tau(\theta) = \frac{(n-1)t}{2nc}\theta^2 + \frac{(4n^2 - n^3 - 3)t}{24n^3c}\theta^4 + ... \tag{A.29}$$

$$= k\theta^2 + k'\theta^4 + ... \tag{A.30}$$

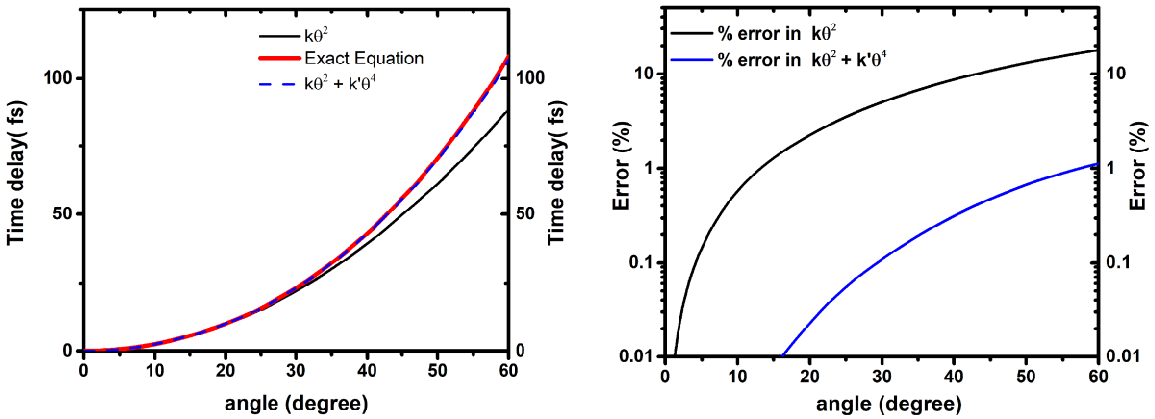

Figure A.3: (Left) Theoretical plot of time delay equation and Taylor's expansion with variation of rotation angle. (Right) The corresponding percentage error in Taylor's expression of first and second order. Here, n is taken as 1.52 , c = 3×10^8 m/s and t is taken as 140 μm.

Theoretical equations for interference intensity

The equation used to fit intensity of fs pulses interference is [57];

$$I(\Delta D) = I_0(1 + e^{-(\frac{\Delta D}{L_{coh}})^2} \cos(\frac{2\pi}{\lambda_0} \times \Delta D)) \tag{A.31}$$

where λ_0 is central wavelength and $L_{coh} = \lambda^2/\Delta\lambda$ is the coherence length of light used. Using equation (A.17), the above equation is fitted for Intensity vs angle (θ) plot.

$$I(\theta) = I_0(1 + e^{-(\frac{t[f(\theta)-\cos\theta]-(n-1)t}{L_{coh}})^2} \cos(\frac{2\pi}{\lambda_0} \times t([f(\theta) - \cos\theta] - (n-1)))) \tag{A.32}$$

Also, Equation (A.31) in terms of time delay (τ) will be,

$$I(\tau) = I_0[1 + e^{-(\frac{\tau}{t_{coh}})^2} \cos(\frac{2\pi c}{\lambda_0} \times \tau)] \tag{A.33}$$

$$= I_0[1 + f(t, \delta t) \cos(\omega_0 \tau)] \tag{A.34}$$

where $f(t, \delta t)$ is pulse envelope and δt is the pulse width.

Note: it is also possible to fit first order autocorrelation function to fs fringes intensity oscillations.

For continuous monochromatic laser, L_{coh} approach to infinity and expression becomes;

$$I(\Delta D) = I_0(1 + \cos(\frac{2\pi}{\lambda_0} \times \Delta D)) \tag{A.35}$$

$$I(\Delta D) = 2I_0 \cos^2(\frac{\pi}{\lambda_0} \times \Delta D) \tag{A.36}$$

Variation in CEP with rotation of glass plate

Rotation of glass plate will also induce a change in carrier envelope phase (ΔCEP). This can be related to optical path delay [4] as;

$$\Delta CEP = 2\pi \frac{\delta n}{\delta \lambda} \times \Delta D \tag{A.37}$$

Plot of variation in CEP in our case

The term $\frac{\delta n}{\delta \lambda}$, also called as chromatic dispersion, is taken from Sellmeier's equation according to reference [96]. $\frac{\delta n}{\delta \lambda} = -0.015721\ \mu m^{-1}$

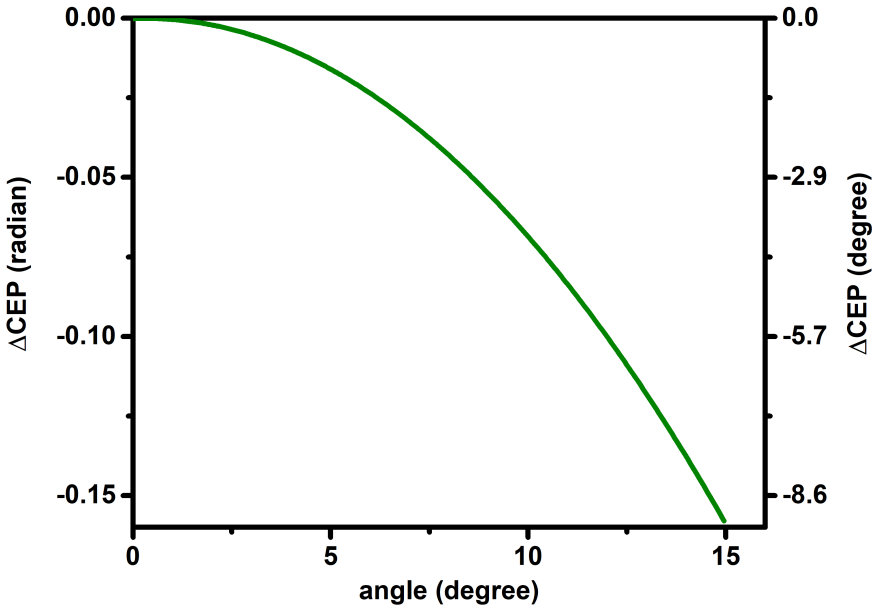

Figure A.4: Change in CEP as function of rotation angle θ. Here, n is taken as 1.52 and t is taken as 140 μm.

Variation in spectrum of light due to ultrathin glasses

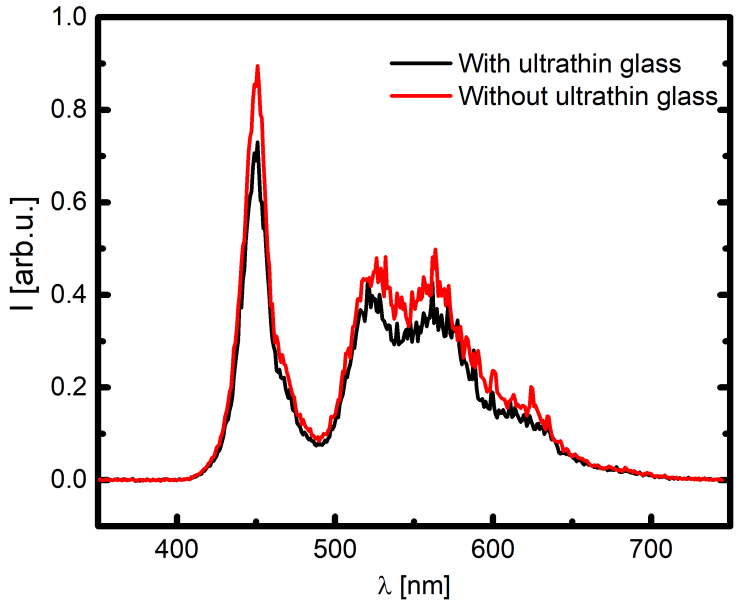

Figure A.5: White LED spectrum with (transmitted) and without ultrathin glasses is measured via Thorlab spectrometer. No significant variation is seen suggesting that ultrathin glass plates (fused silica) can work for wide spectrum specially in white light interferometer.

Bibliography

[1] J. Landers. *Laser Science and Applications*. Willford Press, 2016.

[2] Andrew Weiner. *Ultrafast optics*. John Wiley & Sons, 2011.

[3] A. Douplik et al. "3 - The response of tissue to laser light". In: *Lasers for Medical Applications*. Ed. by Helena Jelínková. Woodhead Publishing Series in Electronic and Optical Materials. Woodhead Publishing, 2013, pp. 47–109. DOI: https://doi.org/10.1533/9780857097545.1.47.

[4] Zenghu Chang. *Fundamentals of attosecond optics*. CRC press, 2016. DOI: https://doi.org/10.1201/b10402.

[5] Ferenc Krausz and Misha Ivanov. "Attosecond physics". In: *Rev. Mod. Phys.* 81 (2009), pp. 163–234. DOI: 10.1103/RevModPhys.81.163.

[6] P. M. Paul et al. "Observation of a Train of Attosecond Pulses from High Harmonic Generation". In: *Science* 292.5522 (2001), pp. 1689–1692. DOI: 10.1126/science.1059413.

[7] Praveen Kumar Maroju et al. "Attosecond pulse shaping using a seeded free-electron laser". In: *Nature* 578.7795 (2020), pp. 386–391. DOI: https://doi.org/10.1038/s41586-020-2005-6.

[8] D. Xiang, Z. Huang, and G. Stupakov. "Generation of intense attosecond x-ray pulses using ultraviolet laser induced microbunching in electron beams". In: *Phys. Rev. ST Accel. Beams* 12 (6 June 2009), p. 060701. DOI: 10.1103/PhysRevSTAB.12.060701.

[9] Sandeep Kumar, Heung-Sik Kang, and Dong-Eon Kim. "For the generation of an intense isolated pulse in hard X-ray region using X-ray free electron laser". In: *Laser and Particle Beams* 30.3 (2012), pp. 397–406. DOI: 10.1017/S0263034612000237.

[10] "Proposal for attosecond light pulse generation using laser induced multiple-harmonic conversion processes in rare gases". In: *Physics Letters A* 168.5 (1992), pp. 447–450. ISSN: 0375-9601. DOI: https://doi.org/10.1016/0375-9601(92)90534-S.

[11] M Hentschel et al. "Attosecond metrology". In: *Nature* 414.6863 (2001), pp. 509–513. DOI: https://doi.org/10.1038/35107000.

[12] Vinzenz Hilbert et al. "An extreme ultraviolet Michelson interferometer for experiments at free-electron lasers". In: *Review of Scientific Instrum.* 84.9 (2013), p. 095111. DOI: 10.1063/1.4821146.

[13] F. Frank et al. "Invited Review Article: Technology for Attosecond Science". In: *Review of Scientific Instrum.* 83.7 (2012), p. 071101. DOI: 10.1063/1.4731658.

[14] Steve Gilbertson et al. "Direct measurement of an electric field in femtosecond Bessel-Gaussian beams". In: *Opt. Lett.* 34.16 (Aug. 2009), pp. 2390–2392. DOI: 10.1364/OL.34.002390.

[15] Jan Tross, Georgios Kolliopoulos, and Carlos A. Trallero-Herrero. "Self referencing attosecond interferometer with zeptosecond precision". In: *Opt. Express* 27.16 (2019), pp. 22960–22969. DOI: 10.1364/OE.27.022960.

[16] M. Huppert, I. Jordan, and H. J. Wörner. "Attosecond beamline with actively stabilized and spatially separated beam paths". In: *Review of Scientific Instrum.* 86.12 (2015), p. 123106. DOI: 10.1063/1.4937623.

[17] Michael Chini et al. "Delay control in attosecond pump-probe experiments". In: *Opt. Express* 17.24 (Nov. 2009), pp. 21459–21464. DOI: 10.1364/OE.17.021459.

[18] Markus Drescher et al. "Time-resolved atomic inner-shell spectroscopy". In: *Nature* 419.6909 (2002), pp. 803–807. DOI: https://doi.org/10.1038/nature01143.

[19] Adrian L Cavalieri et al. "Attosecond spectroscopy in condensed matter". In: *Nature* 449.7165 (2007), pp. 1029–1032. DOI: https://doi.org/10.1038/nature06229.

[20] A. Zaïr et al. "Ultrastable collinear delay control setup for attosecond IR-XUV pump-probe experiment". In: *J. Opt. Soc. Am. B* 35.5 (May 2018), A110–A115. DOI: 10.1364/JOSAB.35.00A110.

[21] H Ahmadi et al. “Collinear setup for delay control in two-color attosecond measurements”. In: *Journal of Physics: Photonics* 2.2 (2020), p. 024006. DOI: https://doi.org/10.1088/2515-7647/ab823f.

[22] Veit Stooß et al. “XUV-beamline for attosecond transient absorption measurements featuring a broadband common beam-path time-delay unit and in situ reference spectrometer for high stability and sensitivity”. In: *Review of Scientific Instrum.* 90.5 (2019), p. 053108. DOI: 10.1063/1.5091069.

[23] E Constant et al. “Toward sub-femtosecond pump-probe experiments: A dispersionless autocorrelator with attosecond resolution”. In: *Le Journal de Physique IV* 11.PR2 (2001), Pr2–537. DOI: https://doi.org/10.1051/jp4:20012105.

[24] FM Böttcher et al. “Interferometric long-term stabilization of a delay line: a tool for pump–probe photoelectron–photoion-coincidence spectroscopy on the attosecond time scale”. In: *Applied Physics B* 91.2 (2008), pp. 287–293. DOI: https://doi.org/10.1007/s00340-008-2987-5.

[25] P Tzallas et al. “Extreme-ultraviolet pump–probe studies of one-femtosecond-scale electron dynamics”. In: *Nature Physics* 7.10 (2011), pp. 781–784. DOI: https://doi.org/10.1038/nphys2033.

[26] R. Trebino et al. “Highly reliable measurement of ultrashort laser pulses”. In: *Journal of Applied Physics* 128.17 (2020), p. 171103. DOI: 10.1063/5.0022552.

[27] Nariyuki Saito et al. “Attosecond streaking measurement of extreme ultraviolet pulses using a long-wavelength electric field”. In: *Scientific reports* 6.1 (2016), pp. 1–5. DOI: https://doi.org/10.1038/srep35594.

[28] Kyung Taec Kim et al. “Photonic streaking of attosecond pulse trains”. In: *Nature Photonics* 7.8 (2013), pp. 651–656. DOI: https://doi.org/10.1038/nphoton.2013.170.

[29] Rick Trebino. *Frequency-Resolved Optical Gating: The Measurement of Ultrashort Laser Pulses*. Springer Science & Business Media, 2000.

[30] Katherine Creath and James C Wyant. “Absolute measurement of surface roughness”. In: *Applied Optics* 29.26 (1990), pp. 3823–3827. DOI: 0.1364/AO.29.003823.

[31] Akiko Harasaki and James C Wyant. “Fringe modulation skewing effect in white-light vertical scanning interferometry”. In: *Applied Optics* 39.13 (2000), pp. 2101–2106. DOI: https://doi.org/10.1364/AO.39.002101.

[32] Seung-Woo Kim and Gee-Hong Kim. "Thickness-profile measurement of transparent thin-film layers by white-light scanning interferometry". In: *Applied Optics* 38.28 (1999), pp. 5968–5973. DOI: https://doi.org/10.1364/AO.38.005968.

[33] Meng-Chi Li, Der-Shen Wan, and Cheng-Chung Lee. "Application of white-light scanning interferometer on transparent thin-film measurement". In: *Applied Opt.* 51.36 (2012), pp. 8579–8586. DOI: https://doi.org/10.1364/AO.51.008579.

[34] Scott Diddams and Jean-Claude Diels. "Dispersion measurements with white-light interferometry". In: *JOSA B* 13.6 (1996), pp. 1120–1129. DOI: DOI:10.1364/JOSAB.13.001120.

[35] IG Cormack, F Baumann, and DT Reid. "Measurement of group velocity dispersion using white light interferometry: a teaching laboratory experiment". In: *American Journal of Physics* 68.12 (2000), pp. 1146–1150. DOI: https://doi.org/10.1119/1.1286664.

[36] Chih-Hung Tsai et al. "Characterizing coherence lengths of organic light-emitting devices using Newton's rings apparatus". In: *Organic Electronics* 11.3 (2010), pp. 439–444. DOI: https://doi.org/10.1016/j.orgel.2009.11.024.

[37] P. A. Young and D. E. O'Connor. "White Light Fringes Obtained with the Michelson Interferometer". In: *American Journal of Physics* 38.12 (Dec. 1970), pp. 1390–1395. DOI: https://doi.org/10.1119/1.1976143.

[38] Max Born and Emil Wolf. *Principles of optics: electromagnetic theory of propagation, interference and diffraction of light*. Elsevier, 2013.

[39] Joanna Schmit and Anna Pakuła. "White Light Interferometry". In: *Handbook of Advanced Nondestructive Evaluation*. Cham: Springer International Publishing, 2019, pp. 421–467. ISBN: 978-3-319-26553-7. DOI: 10.1007/978-3-319-26553-7_42.

[40] Eyal Schwartz. "White light Sagnac interferometer—a common (path) tale of light". In: *European Journal of Physics* 38.6 (2017), p. 065301. DOI: https://doi.org/10.1088/1361-6404/aa8192.

[41] Frédéric Chaussard, Hervé Rigneault, and Christophe Finot. "Two-wave interferences space-time duality: Young slits, Fresnel biprism and Billet bilens". In: *Optics Communications* 397 (2017), pp. 31–38. DOI: https://doi.org/10.1016/j.optcom.2017.03.072.

[42] Pooja Munjal and Kamal P Singh. "A single-lens universal interferometer: Towards a class of frugal optical devices". In: *Applied Physics Letters* 115.11 (2019), p. 111102. DOI: https://doi.org/10.1063/1.5108587.

[43] Evgeny Sysoev et al. "Interferometric surface relief measurements with sub-nano/picometer height resolution". In: *Measurement Science Review* 17.5 (2017), p. 213. DOI: 10.1515/msr-2017-0025.

[44] Jean-Claude Diels and Wolfgang Rudolph. *Ultrashort Laser Pulse Phenomena (Second Edition)*. Academic Press, 2006. DOI: https://doi.org/10.1016/B978-012215493-5/50006-9.

[45] A. McPherson et al. "Studies of multiphoton production of vacuum-ultraviolet radiation in the rare gases". In: *J. Opt. Soc. Am. B* 4.4 (Apr. 1987), pp. 595–601. DOI: 10.1364/JOSAB.4.000595.

[46] M Ferray et al. "Multiple-harmonic conversion of 1064 nm radiation in rare gases". In: *Journal of Physics B: Atomic, Molecular and Optical Physics* 21.3 (Feb. 1988), pp. L31–L35. DOI: 10.1088/0953-4075/21/3/001.

[47] P. B. Corkum. "Plasma perspective on strong field multiphoton ionization". In: *Phys. Rev. Lett.* 71 (13 Sept. 1993), pp. 1994–1997. DOI: 10.1103/PhysRevLett.71.1994.

[48] K. J. Schafer et al. "Above threshold ionization beyond the high harmonic cutoff". In: *Phys. Rev. Lett.* 70 (11 Mar. 1993), pp. 1599–1602. DOI: 10.1103/PhysRevLett.70.1599.

[49] Donna Strickland and Gerard Mourou. "Compression of amplified chirped optical pulses". In: *Optics Communications* 56.3 (1985), pp. 219–221. ISSN: 0030-4018. DOI: https://doi.org/10.1016/0030-4018(85)90120-8.

[50] Esben Witting Larsen. "Attosecond Sources and Interferometers - Developments and Applications". In: *Doctoral thesis* (2016).

[51] Al filter transmission curve. https://lebowcompany.com/transmission-curves.

[52] Christian R. Ott. "Attosecond multidimensional interferometry of single and two correlated electrons in atoms". In: *Doctoral thesis* (2012).

[53] H _ G Muller. "Reconstruction of attosecond harmonic beating by interference of two-photon transitions". In: *Applied Physics B* 74.1 (2002), s17–s21. DOI: https://doi.org/10.1007/s00340-002-0894-8.

[54] Jiro Itatani et al. "Tomographic imaging of molecular orbitals". In: *Nature* 432.7019 (2004), pp. 867–871. DOI: https://doi.org/10.1038/nature03183.

[55] Olga Smirnova et al. "High harmonic interferometry of multi-electron dynamics in molecules". In: *Nature* 460.7258 (2009), pp. 972–977. DOI: https://doi.org/10.1038/nature08253.

[56] Markus Drescher et al. "X-ray Pulses Approaching the Attosecond Frontier". In: *Science* 291.5510 (2001), pp. 1923–1927. DOI: 10.1126/science.1058561.

[57] Niklas Kröger et al. "Using refraction in thick glass plates for optical path length modulation in low coherence interferometry". In: *Applied Opt.* 56.25 (2017), pp. 7299–7304. DOI: 10.1364/AO.56.007299.

[58] Newport. *The Effect of Dispersion on Ultrashort Pulses*. https://www.newport.com/n/the-effect-of-dispersion-on-ultrashort-pulses.

[59] M Rosete-Aguilar et al. "Calculation of temporal spreading of ultrashort pulses propagating through optical glasses". In: *Revista mexicana de fisica* 54.2 (2008), pp. 141–148.

[60] Bluestar. *Cover glasses*. http://bluestarslides.com/cover-glasses.php.

[61] Präzisions glas & optik. *D 263 T*. https://www.pgo-online.com/intl/D263.html.

[62] Ultimaker. *ABS(acrylonitrile butadiene styrene)*. https://ultimaker.com/en/resources/22226-how-to-print-with-ultimaker-abs.

[63] Tracker software. https://physlets.org/tracker/.

[64] Mathematica software. https://www.wolfram.com/mathematica/.

[65] J Herrmann et al. "Multiphoton transitions for delay-zero calibration in attosecond spectroscopy". In: *New Journal of Physics* 17.1 (2015), p. 013007. DOI: 10.1088/1367-2630/17/1/013007.

[66] Qun Zhang and John W. Hepburn. "In situ accurate determination of the zero time delay between two independent ultrashort laser pulses by observing the oscillation of an atomic excited wave packet". In: *Opt. Lett.* 33.16 (2008), pp. 1893–1895. DOI: 10.1364/OL.33.001893.

[67] Sunil Dahiya et al. "In-line ultra-thin attosecond delay line with direct absolute-zero delay reference and high stability". In: *Opt. Lett.* 45.18 (Sept. 2020), pp. 5266–5269. DOI: https://doi.org/10.1364/OL.403842.

[68] Jean-Claude M Diels et al. "Control and measurement of ultrashort pulse shapes (in amplitude and phase) with femtosecond accuracy". In: *Applied Optics* 24.9 (1985), pp. 1270–1282. DOI: https://doi.org/10.1364/AO.24.001270.

[69] Ian A Walmsley and Christophe Dorrer. "Characterization of ultrashort electromagnetic pulses". In: *Advances in Optics and Photonics* 1.2 (2009), pp. 308–437. DOI: https://doi.org/10.1364/AOP.1.000308.

[70] Paraskevas Tzallas et al. "Second-order autocorrelation measurements of attosecond XUV pulse trains". In: *journal of modern optics* 52.2-3 (2005), pp. 321–338. DOI: https://doi.org/10.1080/09500340412331301533.

[71] Christian Spielmann, Lin Xu, and Ferenc Krausz. "Measurement of interferometric autocorrelations: comment". In: *Applied optics* 36.12 (1997), pp. 2523–2525. DOI: https://doi.org/10.1364/AO.36.002523.

[72] Piotr Wasylczyk. "Ultracompact autocorrelator for femtosecond laser pulses". In: *Review of scientific instruments* 72.4 (2001), pp. 2221–2223. DOI: https://doi.org/10.1063/1.1351833.

[73] Nils Fabian Kleimeier et al. "Autocorrelation and phase retrieval in the UV using two-photon absorption in diamond pin photodiodes". In: *Optics express* 18.7 (2010), pp. 6945–6956. DOI: https://doi.org/10.1364/OE.18.006945.

[74] Seong-Il Shin and Yong-Sik Lim. "Simple autocorrelation measurement by using a GaP photoconductive detector". In: *Journal of the Optical Society of Korea* 20.3 (2016), pp. 435–440. DOI: http://dx.doi.org/10.3807/JOSK.2016.20.3.435.

[75] Ida Z Kozma et al. "Compact autocorrelator for the online measurement of tunable 10 femtosecond pulses". In: *Review of Scientific instruments* 75.7 (2004), pp. 2323–2327. DOI: https://doi.org/10.1063/1.1764615.

[76] T Gebert et al. “Michelson-type all-reflective interferometric autocorrelation in the VUV regime”. In: *New Journal of Physics* 16.7 (2014), p. 073047. DOI: http://dx.doi.org/10.1088/1367-2630/16/7/073047.

[77] Pavel V Kolesnichenko, Lukas Wittenbecher, and Donatas Zigmantas. “Fully symmetric dispersionless stable transmission-grating Michelson interferometer”. In: *Optics Express* 28.25 (2020), pp. 37752–37757. DOI: https://doi.org/10.1364/OE.409185.

[78] H Mashiko, A Suda, and K Midorikawa. “All-reflective interferometric autocorrelator for the measurement of ultra-short optical pulses”. In: *Applied Physics B* 76.5 (2003), pp. 525–530. DOI: https://doi.org/10.1007/s00340-003-1148-0.

[79] Ke-Xun Sun and Robert L Byer. “All-reflective Michelson, Sagnac, and Fabry–Perot interferometers based on grating beam splitters”. In: *Optics letters* 23.8 (1998), pp. 567–569. DOI: https://doi.org/10.1364/OL.23.000567.

[80] NA Papadogiannis et al. “Temporal characterization of short-pulse third-harmonic generation in an atomic gas by a transmission-grating Michelson interferometer”. In: *Optics letters* 27.17 (2002), pp. 1561–1563. DOI: https://doi.org/10.1364/OL.27.001561.

[81] Akansha Tyagi et al. “Attosecond stable dispersion-free delay line for easy ultrafast metrology”. In: *Scientific reports* 12.1 (2022), pp. 1–7. DOI: https://doi.org/10.1038/s41598-022-12348-5.

[82] Jean-Claude Diels and Wolfgang Rudolph. *Ultrashort laser pulse phenomena*. Elsevier, 2006.

[83] Matthew Pitkin et al. “Gravitational wave detection by interferometry (ground and space)”. In: *Living Reviews in Relativity* 14.1 (2011), pp. 1–75. DOI: https://doi.org/10.12942/lrr-2011-5.

[84] Clarke K Eastman. “An improved Michelson interferometer: smoothing out the rough spots for a more effective teaching tool”. In: *Education and Training in Optics and Photonics*. Optical Society of America. 2017, 104521H. DOI: https://doi.org/10.1117/12.2269663.

[85] Ankur Mandal et al. “Attosecond delay lines: design, characterization and applications”. In: *The European Physical Journal Special Topics* (2021). DOI: 10.1140/epjs/s11734-021-00261-3.

[86] Pavel Pavliček and Jan Soubusta. "Measurement of the influence of dispersion on white-light interferometry". In: *Appl. Opt.* 43.4 (Feb. 2004), pp. 766–770. DOI: https://doi.org/10.1364/AO.43.000766.

[87] Linlin Zhu et al. "A Novel Surface Recovery Algorithm for Dual Wavelength White LED in Vertical Scanning Interferometry (VSI)". In: *Sensors* 20.18 (2020), p. 5225. DOI: https://doi.org/10.3390/s20185225.

[88] Yuanbo Deng and Daping Chu. "Coherence properties of different light sources and their effect on the image sharpness and speckle of holographic displays". In: *Scientific Rep.* 7.1 (2017), pp. 1–12. DOI: https://doi.org/10.1038/s41598-017-06215-x.

[89] JP Sharpe and DA Collins. "Demonstration of optical spatial coherence using a variable width source". In: *American Journal of Physics* 79.5 (2011), pp. 554–557. DOI: https://doi.org/10.1119/1.3549723.

[90] M. Yanoff, J.S. Duker, and J.J. Augsburger. *Ophthalmology*. Mosby Elsevier, 2009.

[91] Ceyhun Akcay, Pascale Parrein, and Jannick P Rolland. "Estimation of longitudinal resolution in optical coherence imaging". In: *Applied Optics* 41.25 (2002), pp. 5256–5262. DOI: https://doi.org/10.1364/AO.41.005256.

[92] Pavel Pavliček and Ondřej Hbl. "White-light interferometry on rough surfaces measurement uncertainty caused by noise". In: *Applied Opt.* 51.4 (2012), pp. 465–473. DOI: https://doi.org/10.1364/AO.47.002941.

[93] Etalon effect. https://www.azom.com/article.aspx?ArticleID=14009.

[94] Y. C. Chen et al. "Measurement of changes in concentrations of biological solutions using a Rayleigh interferometer". In: *Saratov Fall Meeting 2002: Optical Technologies in Biophysics and Medicine IV*. Ed. by Valery V. Tuchin. Vol. 5068. International Society for Optics and Photonics. SPIE, 2003, pp. 273–283. DOI: https://doi.org/10.1117/12.518786.

[95] Weidong Zhou and Lilong Cai. "An angular displacement interferometer based on total internal reflection". In: *Measurement Science and Technology* 9.10 (1998), p. 1647. DOI: 10.1088/0957-0233/9/10/001.

[96] Mikhail Polyanskiy. *Dispersion in BK7*. https://refractiveindex.info/?shelf=glass&book=BK7&page=SCHOTT.